GeoScienceWorld
Lithosphere
Volume 2023, Article ID lithosphere_2023_279, 21 pages
https://doi.org/10.2113/2023/lithosphere_2023_279

Lithosphere

Research Article

Apatite (U-Th)/He Thermochronological Constraints on the Landscape Evolution Linked to the Normal Faulting in Taishan Mountain, Eastern China

Fangbin Liu[1], **Fan Yang**[2], **Dewen Zheng**[3], **Haiyang Ding**[4], **Caopeng Li**[5] and **Gilby Jepson**[6]

[1]*School of Geography and Tourism, Qilu Normal University, Ji'nan, 250200, China*
[2]*School of Earth Sciences, Lanzhou University, Lanzhou , 730000, China*
[3]*State Key Laboratory of Earthquake Dynamics, Institute of Geology, China Earthquake Administration, Beijing, 100029, China*
[4]*Qingdao Geo-Engineering Surveying Institute, Qingdao, 266101, China*
[5]*Management Committee of Taishan Scenic and Historic Area, Tai'an, 271000, China*
[6]*Department of Geosciences, University of Arizona, Tucson, Arizona, 85721, USA*

Correspondence should be addressed to Fan Yang; fanyang@lzu.edu.cn

Received 14 September 2023; Published 14 February 2024

Academic Editor: Shichao Li

Taishan Mountain in the eastern China is a normal-fault-controlled range that formed during the Meso-Cenozoic, in response to large-scale extension and lithospheric thinning of the North China Craton. However, constraints on the timing of the polyphase extensional events which formed the Taishan edifice remain poorly resolved, hindering a detailed understanding of the landscape evolution of this prominent mountain. Here, we conducted apatite (U-Th)/He dating on sixteen samples from three profiles perpendicular in the Taishan Mountain, with a major view to control structures in Taishan Mountain and to resolve the Meso-Cenozoic landscape evolution. The newly determined apatite (U-Th)/He ages show a wide variation range of ~113 to 30 Ma, indicating a slow and protracted cooling history. The inverse thermal history modeling results reveal two pulses of enhanced cooling at ~80 to 60 and 55 to 50 Ma, which we interpret as exhumation related to normal fault activity. Furthermore, one-dimensional modeling indicates that the magnitude of tectonic exhumation is constrained at ≥15 m/Myr across the Yunbuqiao, Zhongtianmen, and Taishan Piedmont faults. Integrating this study and published studies, we suggest that Taishan Mountain underwent four-stage evolution since 100 Ma: (1) the whole Taishan Mountain commenced a continuous and slow exhumation under a weaker tensional environment at ~100 to 80 Ma, (2) the joint growth and interactions within a normal fault system resulted in rapid uplift and promoted the formation of the Proto-Taishan Mountain at ~80 to 60 Ma, (3) the Taishan Mountain underwent exhumation at ~55 to 50 Ma, interpreted as a tectonic response to the Taishan Piedmont Fault, and (4) the last stage (~50 to 0 Ma), the Taishan Mountain experienced protracted exhumation related to normal faulting until now. We attribute the extensive normal faulting to the subduction and slab rollback of the Izanagi-Pacific Plates, which shaped the present-day geomorphology of Taishan Mountain.

1. Introduction

Since the Late Mesozoic, normal faulting has been thoroughly documented in the eastern province of the North China Craton (NCC) [1–3]. The development of extensional systems has been widely recognized as a critical aspect of redistributing thickened crust following orogenesis and plays a significant role in shaping relief [4–6]. The eastern margin of the NCC hosts numerous large-scale normal faults; thus, how the extensional regime evolves through time is fundamental for understanding the landscape evolution of eastern China. Although these processes of fault growth have been studied extensively in understanding the patterns of subsidence within hanging

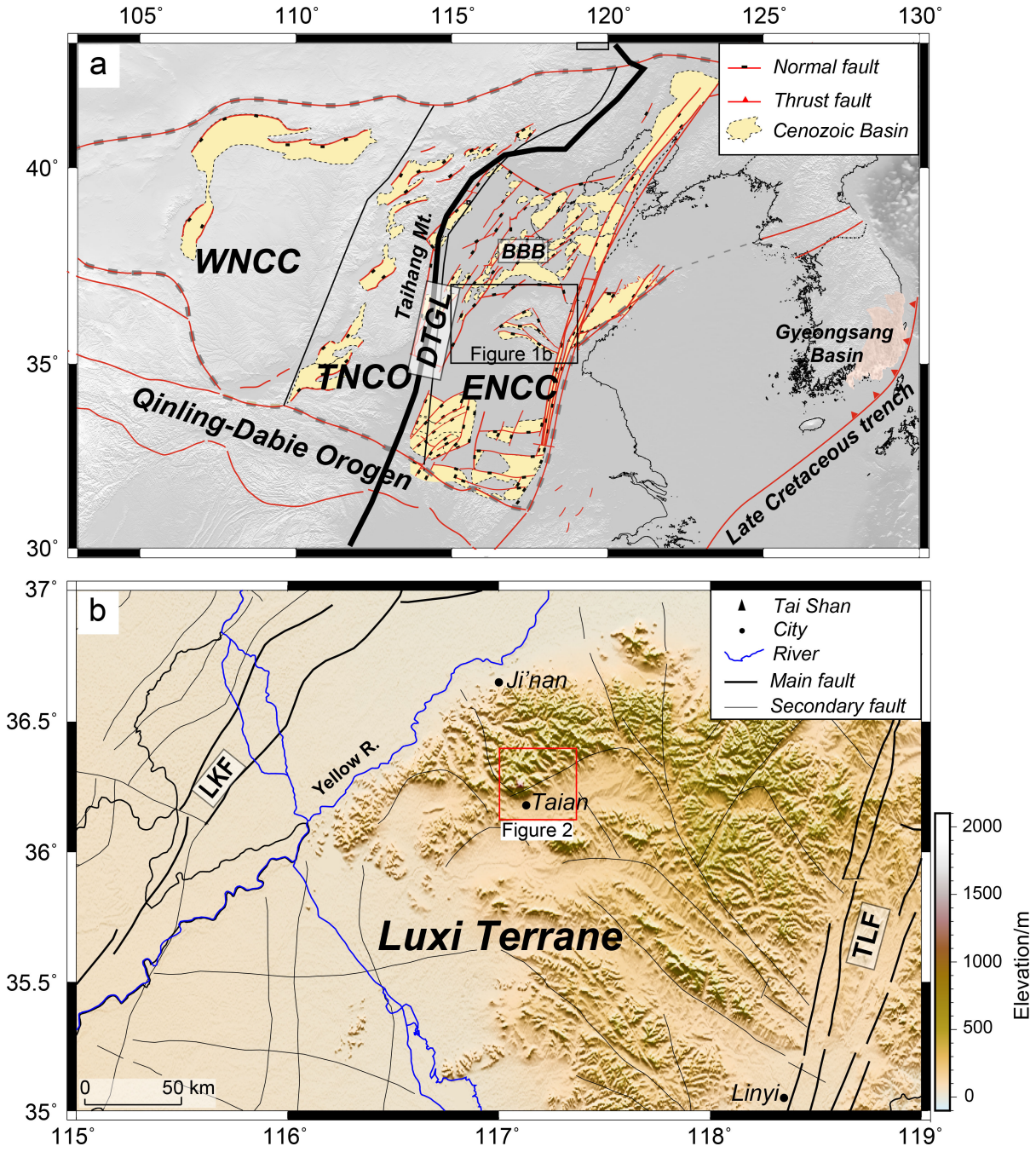

FIGURE 1: (a) Simplified tectonic and geological map of the North China Craton (modified from Yang et al. [131] 2018, Zhang et al. [25], and Zhu et al. [132]). (b) Region tectonic framework of Luxi Terrane, China. BBB, Bohai Bay Basin; DTGL, Daxing'anling–Taihangshan Gravity Lineament; ENCC, Eastern North China Craton; LKF, Liaocheng–Lankao Fault; TLF, Tan–Lu Fault; TNCO, Trans-North China Orogen; WNCC, Western North China Craton.

walls of rift-basin systems [7–12], there remain few studies that focus on how fault growth influences the tectonic development of the preserved topography.

The Taishan Mountain within the eastern NCC is a large extensional range that was established through a sequence of parallel normal faults (Figures 1 and 2) [13, 14]. These faults formed three step-type geomorphic landscapes that exert a first-order control over the formation of (East-Northeast) ENE-trending extensional basins and Cenozoic deposits [14, 15]. In addition, Lv [16] also suggested that the Yanshanian (Late Jurassic to Early Cretaceous) tectonic episodes played a key role in determining the Late Mesozoic tectonic evolution of the Taishan Mountain. In recent decades, several studies focused on the extensional tectonics, uplift history, and exhumation rate of Taishan, yet the timing and mechanism of uplift of this range are still unclear. Based on apatite fission track (AFT) data, Li and Zhong [17] and Li

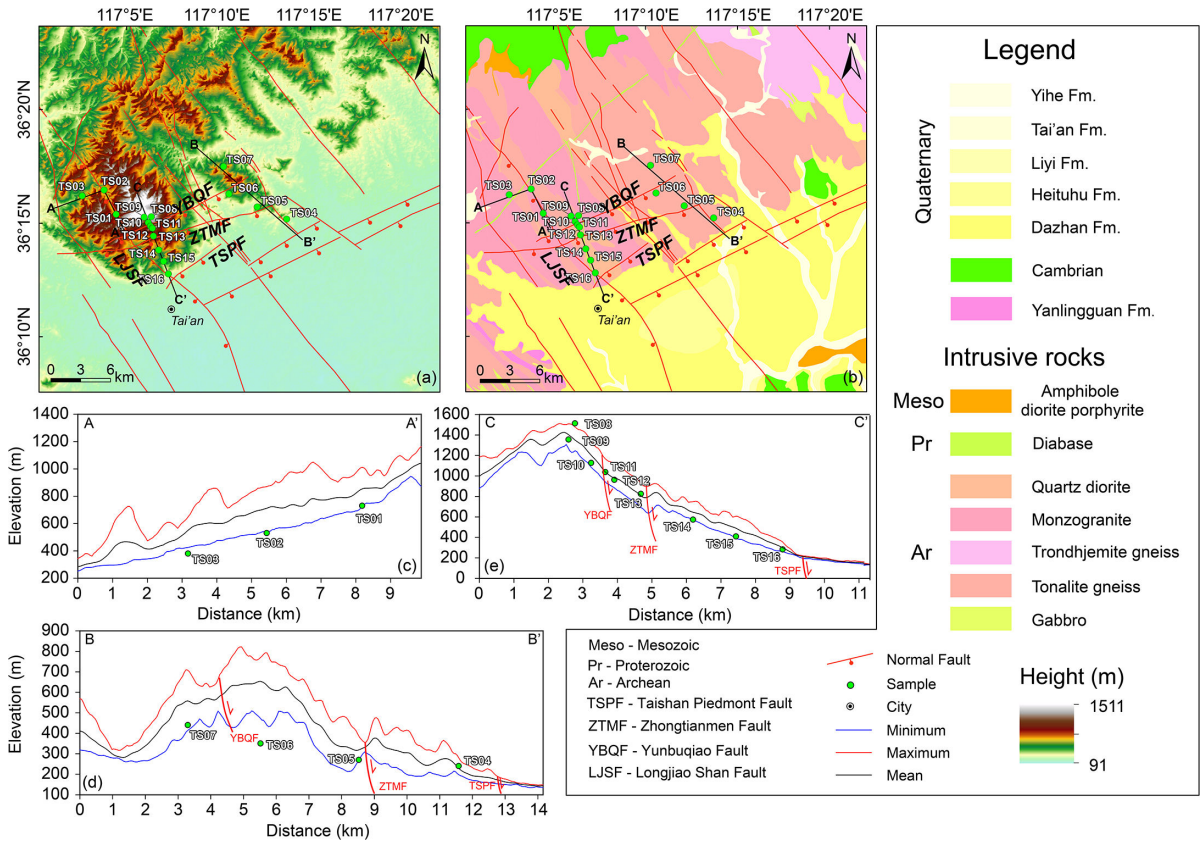

FIGURE 2: (a) Topographic and (b) geological maps of the Taishan Mountain with sample location. The swath profiles of (c) Transect A, (d) Transect B, and (e) Transect C are calculated using a 1 km width.

et al. [18, 19] suggested that Taishan Mountain initiated exhumation at the Early Cenozoic and shaped the current landscape at Miocene, in response to the combined effects of the India–Eurasia collision and the subduction of the Pacific Plate. However, many of these AFT data indicated partial reset which suggested that total exhumation would have to be less than 4–6 km [20]. Thus, in order to resolve the tectonic evolution of Taishan Mountain, a low-temperature thermochronometer that is sensitive to lower temperatures than AFT is required.

Apatite (U-Th)/He thermochronology (AHe) is a popular and well-established tool for directly determining the exhumation timing of bedrocks correlated with normal faulting [11, 21–25]. Specifically, the AHe dating hosts a low closure temperature and is more sensitive to thermally activated volume diffusion within a partial retention zone of ~40°C to 80°C [26, 27]. Therefore, it has been widely applied to constrain the landscape evolution and tectonic history of terrains within the upper crust (2, 4 km) [28, 29]. Furthermore, the thermochronological sampling strategy highly depends on the regional deformation pattern [22, 23]. Thus, in order to constrain the tectonic evolution of Taishan Mountain, we carried out single-grain AHe dating on forty-eight representative apatite grains from sixteen samples across the normal fault system along three transects in the Taishan region. Joining the thermal inversion of these thermochronological data, our major objectives are to determine the formation timing and motion rate of normal faults and to constrain the landscape evolution of Taishan Mountain. Moreover, this study also will provide related insights into geodynamic mechanisms for exhumation throughout the whole eastern NCC.

1.1. Tectonic Setting. Taishan Mountain, a prominent secondary unit in Luxi Terrane, is located in the western section of the tectonic activity zone of eastern NCC (Figure 1). It is commonly explored for geological resources and preserves abundant geological occurrences, such as emplacement of basic and tonalitic magmas, and post-magmatic deformation and metamorphism [13, 30]. The Taishan Association (Archean crystalline basement rock) is partially overlain by Paleoproterozoic to Cenozoic platform cover, which makes up the main body of Taishan Mountain (Figure 2) [31]. Basement gneisses and granitoid intrusions comprise the main Taishan Association's rock assemblage [30, 32]. Gray gneisses and amphiboles are found in various amounts in the basement gneisses [30]. The Trondhjemite, Tonalite, and Granodiorite gneisses dominate the granitoid intrusions and contain interlayered leucosome and melanosome bands which have been interpreted to be a result of anatexis (Figure 2) [32]. From bottom to top, this association developed greenschist to amphibolite facies metamorphism and was classified into Yanlingguan, Shancaoyu, and Liuhang formations [33]. Based on zircon U-Pb dating analysis, previous geochronological studies

have suggested that the Taishan Association was formed at 2.7 Ga [34, 35].

The Taishan Mountain is dominated by ENE and NW trending faults (Figure 2) [10, 18, 36, 37], which play a key role in the exhumation of Taishan and its geomorphic pattern [13, 14]. The NW trending faults, such as the Longjiao Shan Fault, were generated and developed under almost E-W horizontal stress during the Mesozoic [37]. These faults show strike 320°–340° and dip 60°–80° SW, with 50–100 m in width [10, 37, 38]. In contrast, the ENE trending faults, including Yunbuqiao Fault (YBQF), Zhongtianmen Fault (ZTMF), and Taishan Piedmont Fault (TSPF), are largely confined to the southern part of the Taishan Mountain (Figure 2). These faults yield dip angles that are approximately vertical toward the SSE direction [13, 14, 16]. Moreover, these three faults include distinctive step-type geomorphic landscapes that exert some control over the formation of ENE-trending extensional basins and Cenozoic deposits [13–16]. Previous studies have analyzed the Cenozoic cooling history of the Taishan Mountain [17, 19, 39] and suggest that the Taishan Mountain underwent at least three periods of rapid cooling events, including Early Eocene, Mid-Late Eocene, and Early Miocene. The overall uplift of Taishan Mountain is believed to have reached more than 500 m since the Quaternary, with a rate of 0.5 mm/y [13, 40].

2. Sampling and Methodology

2.1. Sampling. A total of sixteen granite samples were collected from three transects within the Taishan Mountain (Figures 2(a) and 2(b)). A hand Global Positioning System (GPS) was employed to determine the location and elevation of each sample. See Table 1 for a complete list of sample descriptions.

Transect A is located at the western segment of Taishan Mountain and includes three samples with elevations varying from 730 to 380 m (Figure 2(c)). Transect B is about 10 km in the east of Transect A. Four samples were collected from an almost horizontal profile (Transect A), with elevation extending from 440 to 240 m over the YBQF and ZTMF (Figure 2(d)). Transect C presents a shape of the NNW-SSE route between Transect A and Transect B. From the top of the Jade Emperor Peak (Yuhuangding in Chinese) to the bottom, nine samples are collected along an elevation profile, which covers 1231 m relief over a lateral extent of ~7 km (Figure 2(e)).

2.2. Apatite (U-Th)/He Analysis. First, apatite separation was extracted using standard crushing, sieving, electromagnetic, and heavy liquid mineral separation techniques. Following that, the apatite grains were hand-picked under a high-power stereographic microscope. Only inclusion-free, euhedral, unfractured, and large grains were selected. Finally, the AHe analysis was conducted at the Institute of Geology, China Earthquake Administration. The analytical procedure mainly includes helium extraction wrapped in the Pt capsule and measurement of U and Th contents by inductively coupled plasma mass spectrometer, following the description by Yu et al. [41]. For more detailed experimental protocols, see Text S1 in the supplementary material.

During this analysis, we selected Durango apatite as a reference standard to test our analytical technique. Replicating analyses of twelve Durango apatite grains yielded AHe ages in the range of 33.7–29.2 Ma, with an average age of 31.5 ± 1.1 Ma (online Supplementary Figure S1). This is consistent with the reported reference of 31.02 ± 0.22 Ma [42].

2.3. Thermal History Modeling. In this study, QTQt software is applied to construct the thermal history modeling [43]. The QTQt software could identify the optimal time–temperature (t–T) path from thermochronological ages for single or multiple samples based on the Bayesian transdimensional Markov chain Monte Carlo (MCMC) inversion scheme [43]. For each transect, we first modeled the thermal history of each sample individually and then modeled multiple samples in the same wall of faults together as an integrated vertical transect.

During modeling, we used the radiation damage accumulation and annealing model of Flowers et al. [44] for helium diffusion in apatite. Similarly, geological restrictions are also taken into account in this modeling: (1) considering the effect of the range of the prior distribution on time and temperature, the oldest age is defined as the center of time, with a range of plus/minus oldest aliquot age, and the temperature range was centered on 70°C with a range of ±70°C, (2) a present-day mean temperature of 14°C ± 14°C are selected for all samples [17], and (3) the geothermal gradient of 36°C/km are adopted [17]. In addition, temperature offsets are allowed to change over time due to the possibility of alterations in the paleogeothermal gradient. For all modeling samples, we did not employ any extra constraints. All models represented 200,000 iterations: 100,000 for the burn-in, and the subsequent 100,000 accepted models for the posterior ensemble. Exploratory runs with larger numbers could not appreciably change model outcomes.

3. Results

3.1. Apatite (U-Th)/He Dating. A total of forty-eight apatite grains were analyzed for AHe ages, the newly obtained age data are given in Table 1. Due to the analytical inconsistency of measurements and outlier thermal histories compared with the rest replicates for the same sample, individual apatite grain ages are excluded in this study (Table 1 and online Supplementary Figure S2). The AHe dates are much younger than the corresponding crystallization ages [34, 35], indicating that these samples have been reset. Furthermore, there is no relationship observed between elevation and AHe ages for three transects (Figure 3).

Transect A contains three samples, the lowest elevation sample (TS03) yields the youngest AHe mean age of 40.2 ± 0.7 Ma, whereas the highest elevation sample (TS01) shows

Table 1: Apatite (U-Th)/He thermochronological data of three transects in the Taishan Mountain.

Sample	U	Th	eU[1]	[4He]	Radius		Corr. age	±1σ	Mean age[3]	Latitude	Longitude	Elevation
no.	(ppm)	(ppm)	(ppm)	(nmol/g)	(μm)	Ft[2]	(Ma)	(Ma)	(Ma ± 1σ)	(°N)	(°E)	(m)
TS01-1	8.37	10.34	10.80	3.0709	51.85	0.73	71.8	1.7	64.4 ± 1.1	36°15′23″	117°4′25″	730
TS01-2	13.88	12.66	16.85	3.7194	43.83	0.68	59.3	1.4				
TS01-3[4]	0.90	11.63	3.63	1.4465	41.22	0.64	113.4	3.9				
TS02-1	6.81	1.81	7.24	2.3432	73.83	0.81	73.5	1.4	74.0 ± 1.2	36°16′27″	117°3′46″	530
TS02-2[4]	3.27	1.50	3.62	1.4806	76.12	0.81	92.1	1.9				
TS02-3	5.74	6.99	7.38	2.0545	43.36	0.68	75.2	2.1				
TS03-1[4]	0.82	9.80	3.13	0.3784	57.85	0.74	30.1	0.6	40.2 ± 0.7	36°16′12″	117°2′8″	380
TS03-2	1.20	8.79	3.26	0.5397	64.96	0.77	39.6	0.8				
TS03-3	1.40	9.21	3.57	0.5610	46.31	0.68	42.2	1.5				
TS04-1[4]	9.69	9.30	11.87	4.1485	64.72	0.78	82.2	1.5	62.3 ± 1.1	36°15′11″	117°13′42″	240
TS04-2	4.68	4.67	5.77	1.3422	42.38	0.67	63.4	1.8				
TS04-3	4.51	6.71	6.09	1.5792	62.68	0.77	61.8	1.3				
TS05-1	8.29	5.11	9.49	2.5842	90.15	0.84	59.5	1.1	60.2 ± 0.7	36°15′43″	117°12′5″	270
TS05-2	8.40	3.51	9.23	2.5319	69.35	0.80	63.3	1.3				
TS05-3	10.48	3.89	11.39	2.8372	66.86	0.79	58.0	1.3				
TS06-1	19.58	1.52	19.94	6.1156	69.64	0.80	70.5	1.5	72.0 ± 0.9	36°16′15″	117°10′33″	350
TS06-2	16.02	4.33	17.03	5.5629	79.56	0.82	72.9	1.4				
TS06-3	8.54	0.99	8.78	2.8429	77.22	0.82	72.7	1.6				
TS07-1	18.08	12.99	21.13	5.9515	94.25	0.85	61.1	1.0	57.7 ± 0.7	36°17′30″	117°10′16″	440
TS07-2	6.51	4.50	7.57	1.6518	50.13	0.72	55.5	1.6				
TS07-3	7.72	5.12	8.92	1.9095	59.83	0.76	51.5	1.2				
TS07-4	1.74	3.19	2.49	0.6651	56.42	0.75	65.8	2.2				
TS08-1[4]	9.69	29.01	16.51	7.0569	74.13	0.80	97.9	1.6	72.4 ± 1.0	36°15′17″	117°6′21″	1513
TS08-2	19.41	18.35	23.72	6.9268	51.59	0.73	73.7	1.3				
TS08-3	4.11	10.20	6.51	2.0122	74.39	0.80	70.7	1.5				
TS09-1	2.83	11.37	5.50	1.4907	48.60	0.70	70.9	1.7	65.3 ± 1.2	36°15′16″	117°5′57.75″	1355
TS09-2[4]	3.16	9.22	5.33	2.0462	63.95	0.77	91.4	2.1				
TS09-3	2.14	8.42	4.12	0.9467	48.40	0.70	60.3	1.6				
TS10-1	3.32	7.20	5.01	1.3908	59.58	0.76	67.3	1.2	66.9 ± 0.8	36°15′0.99″	117°6′10.05″	1127
TS10-2	4.93	7.51	6.70	2.0381	81.20	0.82	68.1	1.3				
TS10-3	4.23	7.52	5.99	1.7064	74.02	0.80	65.1	1.4				
TS11-1	1.92	6.78	3.51	1.5522	71.49	0.79	102.2	2.2	104.8 ± 1.7	36°14′52.23″	117°6′17.41″	1037
TS11-2	1.36	5.66	2.69	1.2471	68.48	0.78	108.7	2.7				
TS12-1	1.40	5.33	2.65	1.0882	68.80	0.78	95.9	2.3	87.9 ± 1.4	36°14′45.66″	117°6′25.95″	962
TS12-2	1.43	4.51	2.49	0.9354	85.20	0.82	83.6	1.7				
TS13-1	17.28	33.35	25.12	5.5967	59.54	0.76	54.1	0.9	54.6 ± 0.5	36°14′26.16″	117°6′26.88″	824
TS13-2	7.20	9.00	9.31	2.0969	54.68	0.74	55.8	1.4				
TS13-3	10.99	24.32	16.71	3.7749	50.26	0.71	58.0	1.1				
TS13-4	10.44	24.32	16.15	3.5480	63.35	0.77	52.4	0.9				
TS14-1	3.61	8.84	5.69	2.0877	62.87	0.77	87.6	1.8	81.2 ± 1.2	36°13′49.08″	117°6′43.34″	573
TS14-2	5.17	6.68	6.74	2.2796	75.40	0.81	76.7	1.5				
TS14-3[4]	1.95	5.57	3.26	0.7283	78.77	0.81	50.6	1.1				
TS15-1	4.01	20.21	8.76	1.1788	35.75	0.60	41.1	0.9	41.2 ± 0.6	36°13′18.98″	117°6′58.96″	409

(*Continued*)

Table 1: Continued

Sample	U	Th	eU[1]	[4He]	Radius		Corr. age	±1σ	Mean age[3]	Latitude	Longitude	Elevation
no.	(ppm)	(ppm)	(ppm)	(nmol/g)	(μm)	Ft[2]	(Ma)	(Ma)	(Ma ± 1σ)	(°N)	(°E)	(m)
TS15-2[4]	4.41	23.08	9.84	1.7484	41.36	0.65	50.3	1.2				
TS15-3	4.65	25.27	10.59	1.5958	44.19	0.67	41.3	0.8				
TS16-1	4.24	19.52	8.83	2.0357	72.42	0.79	53.4	0.9	57.0 ± 0.6	36°12′47.13″	117°7′15.09″	282
TS16-2	5.76	30.73	12.98	3.0643	56.90	0.74	58.6	1.0				
TS16-3	3.95	17.73	8.11	1.9570	49.95	0.71	62.6	1.4				

[1]Effective uranium content, eU = U + 0.235 × Th.

[2]α-ejection correction [53] calculated using mass-weighted mean radius.

[3]The weighted mean age calculation using the Isoplot of Ludwig [133].

[4]These aliquots were excluded in the modeling process and outlier, see text for explanation.

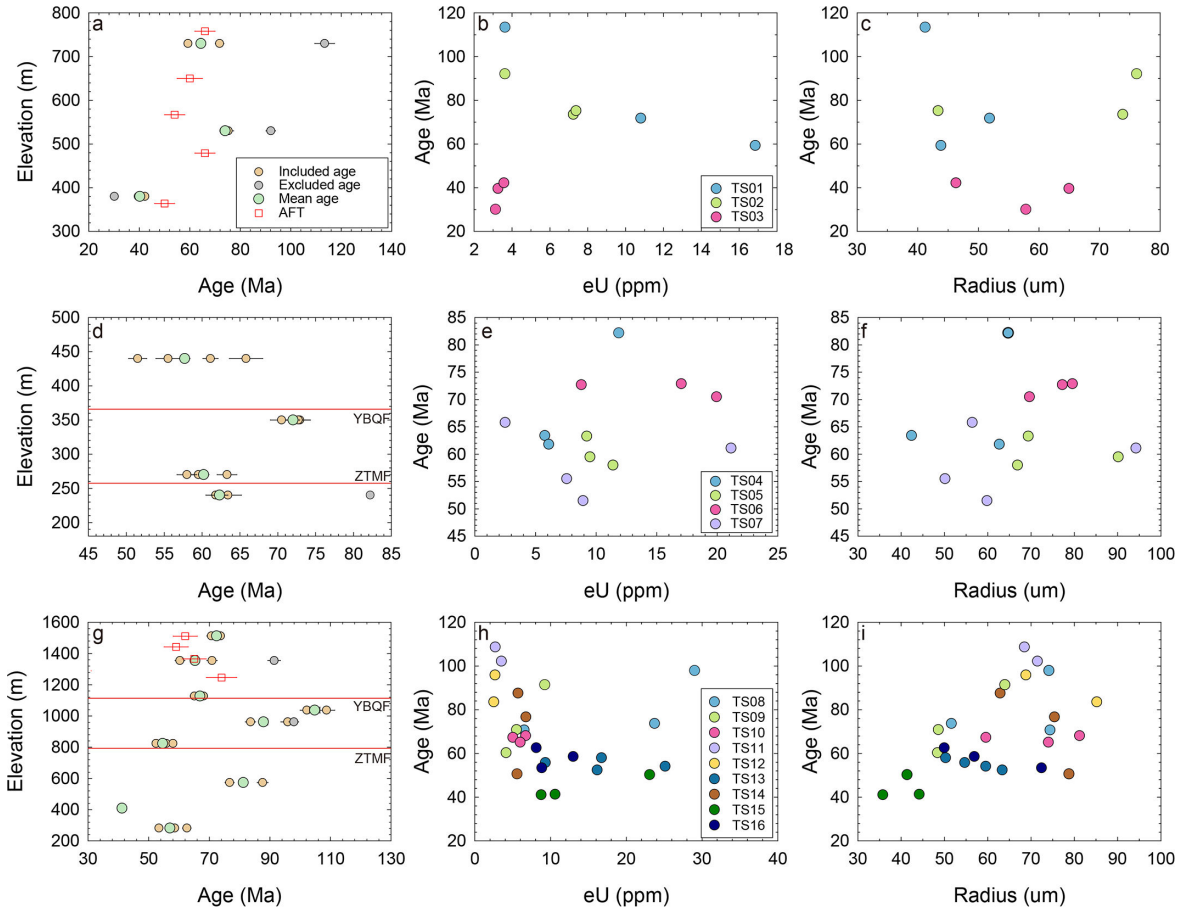

Figure 3: Corrected AHe ages versus elevations (left), effective uranium content [eU] (center), and equivalent sphere radius (right) from Transect A (a–c), Transect B (d–f), and Transect C (g–i), respectively. The red lines in the left column present the fault planes. TSPF, Taishan Piedmont Fault; YBQF, Yunbuqiao Fault; ZTMF, Zhongtianmen Fault. The AFT data are derived from Tang [39].

a mean age of 64.4 ± 1.1 Ma (Figure 3(a)). These ages overlap with published AFT ages by Tang [39].

Transect B includes four samples and yields AHe mean ages ranging from 72.0 ± 0.9 to 57.7 ± 0.7 Ma (Table 1 and Figure 3(d)). More specifically, the AHe ages with higher elevation samples (TS05 and TS07) are younger than those at lower elevations (TS04 and TS06; Figure 3(d)).

For Transect C, nine samples were collected along the section with a vertical elevation profile which crossed the ZTMF and YBQF (Figure 2(e)). These samples yield the AHe mean ages varying from 104.8 ± 1.7 to 41.2 ± 0.6 Ma (Table 1 and Figure 3(g)). The reproducibility of the single grains for each sample is inhomogeneous from one sample to another. The transect is further divided

into three segments by the ZTMF and YBQF (Figures 2(e) and 3(g)). In the footwall of the YBQF, three samples yield similar ages, ranging from 72.4 ± 1.0 to 65.3 ± 1.2 Ma. These AHe grain ages also overlap with previously published AFT data [39], which may represent a rapid cooling episode during this period. Between the ZTMF and YBQF, three samples are collected and show a distinct age-elevation gradient variation with ages declining from 104.8 ± 1.7 to 54.6 ± 0.5 Ma. In the hanging wall of the ZTMF, the analyzed AHe ages are shown between 81.2 ± 1.2 and 41.2 ± 0.6 Ma.

Furthermore, the single-grain AHe ages of several intrasamples show distinct dispersion variations (Table 1 and Figure 3). In general, this dispersion would reflect differences in the properties of the grains that influence the He diffusion kinetics [45]. In order to explore the main factors that influence the dispersion of data, we will further clarify in the following text (see detailed discussion).

3.2. Thermal History Modeling. For Transect A, given the samples were not collected along the elevation transect, individual thermal history modeling was conducted. The inversion results indicate that two higher elevation samples (TS01 and TS02) show similar t–T paths, interpreted as an enhanced exhumation event during ~80 to 60 Ma. In contrast, the low sample (TS03) underwent cooling at ~40 Ma (Figure 4). Almost all thermal history models from Transect A show consistency between observed and predicted values [46]. However, the variation trends in the predicted values of TS03 are characterized by significant differences from the corresponding observations, and we assess that the t–T path of this sample is not well constrained.

Four individual models in Transect B (TS04–TS07) show a similar cooling history, with a three-stage thermal history since the Late Cretaceous. The initial stage was a slow cooling phase until ~80 Ma, followed by a rapid cooling in which all the samples passed through the apatite He partial retention zone (AHePRZ). This was followed by slow, monotonic cooling after ~50 Ma (~40 Ma for TS07) until the present day (Figure 4). We suggest that the 80–50 Ma enhanced cooling may be correlated with the TSPF, as these samples are located in the footwall of TSPF (see detailed discussion). Furthermore, the multisample inverse thermal history modeling indicates two rapid cooling events (Figure 5a). The early cooling event started at ~80 Ma and caused ~40°C cooling, consistent with the cooling event revealed by individual samples (Figure 4). Following a protracted period of minor reheating, a second period of cooling occurred from 10 Ma to the present, with a cooling rate of ~2°C/Myr. However, this cooling event was not resolved by the individual samples (Figure 4). It is well known that AHe thermochronology is sensitive to capturing the thermal history of AHePRZ (80°C–40°C). We also found that the temperature, at which the last cooling event was recorded, was above the AHePRZ. In addition, the AHe age of the low sample (TS05) was poorly predicted and significantly older than the corresponding age. Thus, we do not further consider the rapid cooling from 10 Ma to the present. It also further suggests that the Late Cretaceous to Early Cenozoic AHe data could not accurately constrain the rapid cooling event during the Late Cenozoic.

The individual models from Transect C present a single pulse of cooling (Figure 4). The samples TS08–TS10 in the footwall of the YBQF both indicated an Early Cenozoic rapid cooling at ~80–60 Ma, followed by slow and protracted cooling until the present. The integrated transect model result is consistent with these individual models, indicating a major cooling pulse of 50°C–60°C during ~80 to 60 Ma (Figure 5(b)). The coupling between individual and multisample models further clarifies that these modeling results show identical rapid cooling at ~80 to 60 Ma, which is also similar to the interpretation from the age-elevation relationship (Figure 3(g)).

In contrast, the individual models of samples TS11–TS13 between YBQF and ZTMF display different t–T paths. Sample TS11 with the oldest AHe age (104.8 ± 1.7 Ma) reveals an earlier and more modest cooling episode between ~120 and 100 Ma. Sample TS12 captures a Late Cretaceous rapid cooling event at ~90 to 80 Ma, followed by a slow cooling or quiescence period until the present (Figures 4 and 2). Additionally, a late fast cooling episode until ~50 Ma is captured by sample TS13. Considering that the variation between predicted and observed dates of these samples can hamper the accurate t–T paths (Figure 4), we carried out a multisample inversion (Figures 5(c) and 3). The inverse modeling results with/without TS11 imply a uniform thermal history, which means one anomalous age that does not have much influence on the model results. In this case, the thermal history is resolved back to ~100 Ma. There is a minor reheating event until ~50 Ma, followed by accelerated cooling from 40°C to 60°C to near the surface. Subsequently, a period of apparent quiescence is at ~50 Ma to the present day (Figures 5(c) and 3).

Samples TS14–TS16 which were in the hanging wall of ZTMF (or in the footwall of TSPF) indicate a comparable cooling history (individual and multisample models) to those samples (TS11–TS14; Figures 4 and 5). This suggests that the YBQF and ZTMF may have experienced a similar thermal evolution since ~100 Ma. We also note that the samples with two walls of the YBQF underwent an opposite exhumation history during the ~80–60 Ma (Figures 5(b) and 5(c)). The result indicated that the enhanced activity of YBQF and ZTMF initiated during this period and controlled the relative motion of the walls. In addition, the Early Cenozoic rapid cooling phase presented in Figures 5(c) and 5(d) may be affected by TSPF. During ~55 to 50 Ma, the TPSF underwent more intense tectonic activity than YBQF and ZTMF, resulting in the blocks between YBQF and TSPF changing from relative subsidence to relative uplift (see detailed discussion).

The thermal history models of single and multiple samples were not always compatible, which shows some differences along the entire t–T paths (Figures 4 and 5). This phenomenon was observed not only in our study area but also in other areas [7, 11]. Abbey et al. [47] proposed this discrepancy might result from

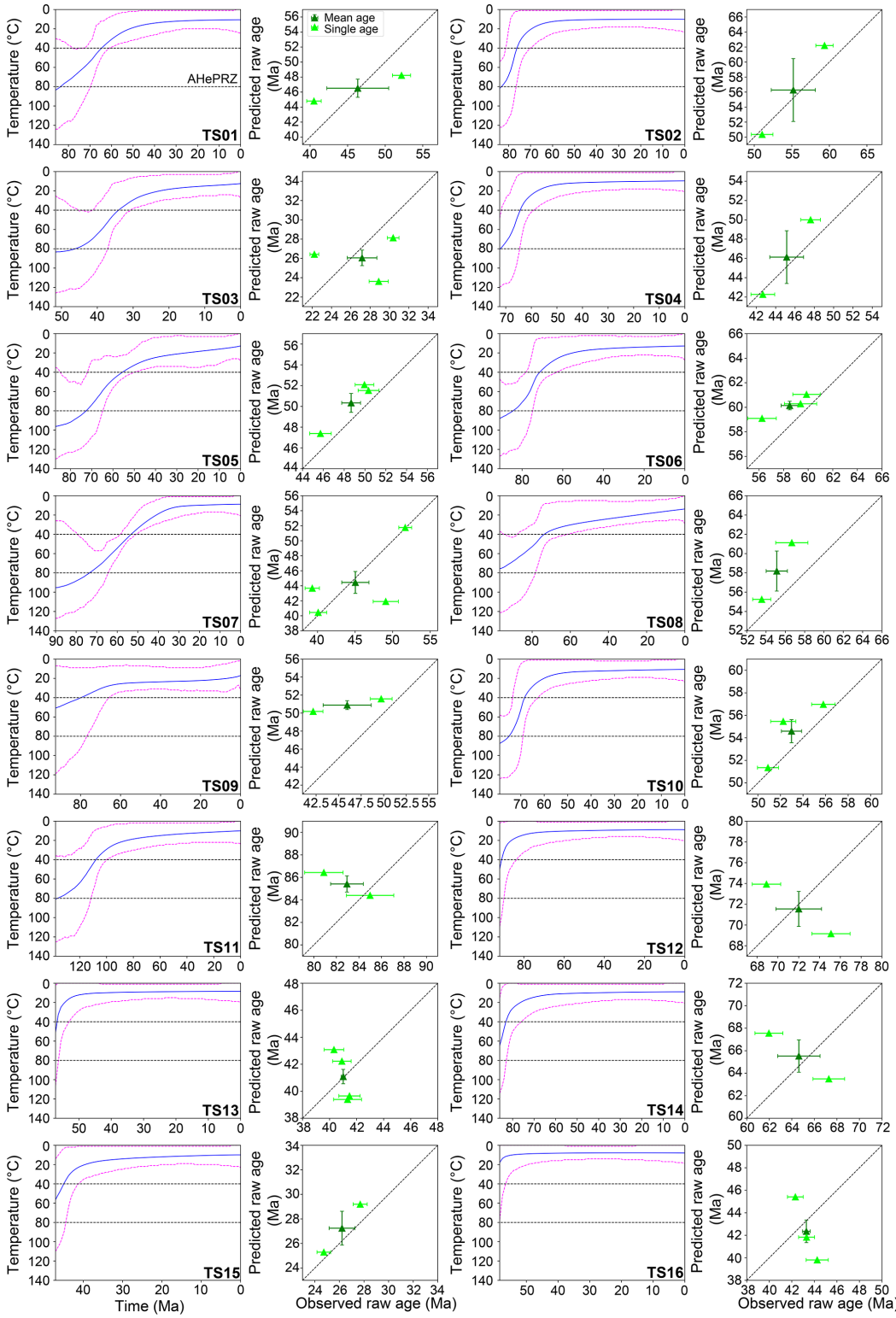

FIGURE 4: Thermal history models of individual samples calculated by the QTQt after the exclusion of anomalous grains. Left column: the magenta dotted lines show 95% credible intervals for the expected model, and the blue solid lines represent best-fit models to analytical data. Right column: the relationship between observed and predicted raw ages. AHePRZ, apatite He partial retention zone.

the modeling strategy of the QTQt. QTQt utilizes the MCMC method to determine the optimal t–T path based on thermochronological ages of single or multiple samples [43]. As a result, the thermal history model solutions inherently lack uniqueness. Moreover, each modeling result illustrated a single pulse of the cooling event (e.g., Figures 4 and 2) since QTQt favored simpler models to avoid over-interpretation of

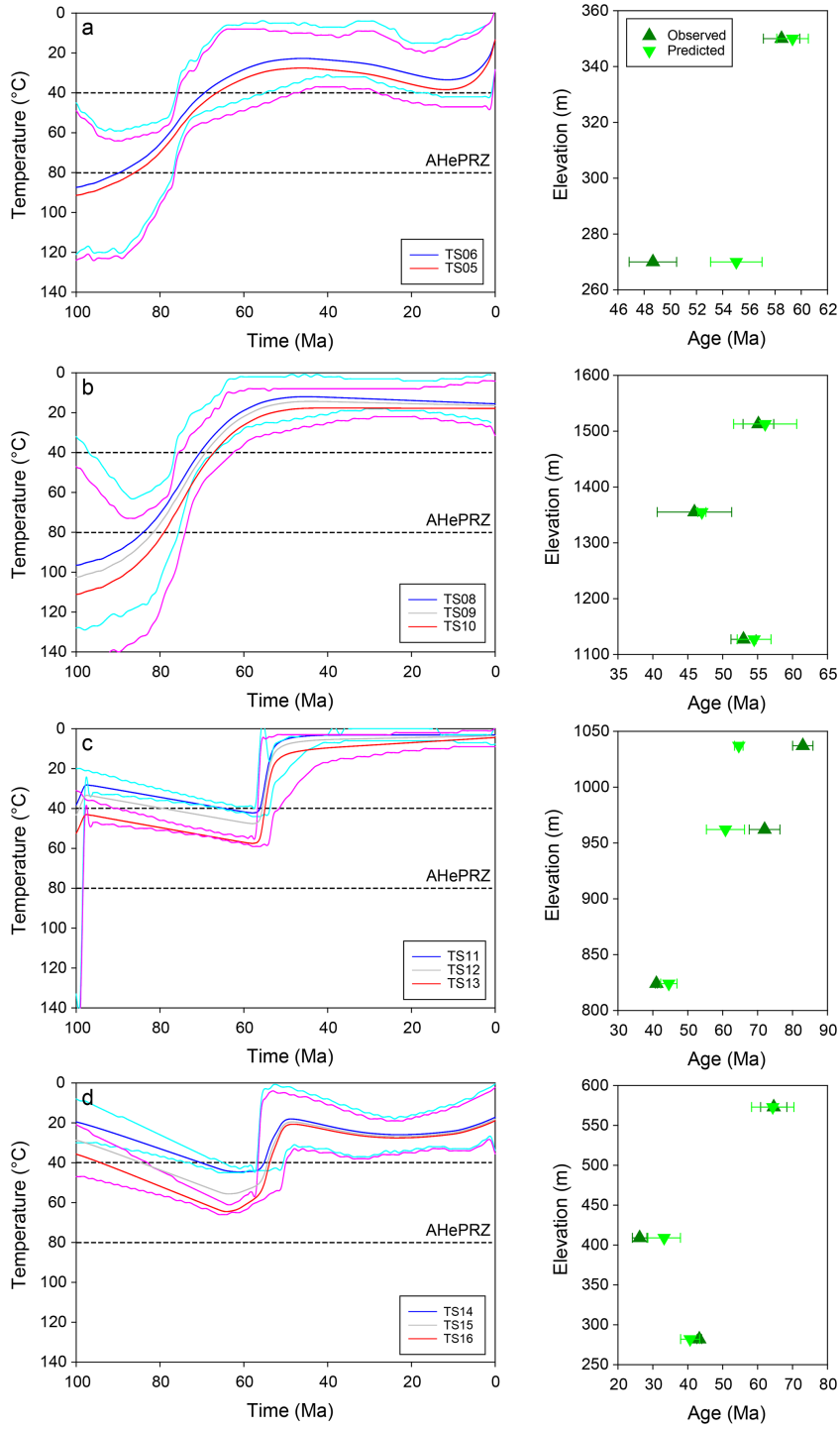

FIGURE 5: Thermal history models of multiple samples calculated by the QTQt. The cyan and magenta lines are the 95% credible intervals about the coldest (blue line) and hottest (red line) sample thermal histories. The gray lines represent the samples between the coldest and hottest samples. Right column: the relationship between mean observed and predicted raw ages. AHePRZ, apatite He partial retention zone.

available data [43]. Therefore, it is essential to conduct a multisample inversion along an elevation transect, as it may provide a more comprehensive or intricate understanding of thermal histories compared with a single sample.

However, all results demonstrated overlapping cooling events between the individual and grouped thermal history models. Overall, we conclude that Taishan Mountain underwent a multistage exhumation history since the Late Cretaceous (Figures 4 and 5). Before 80

Ma, the whole Taishan Mountain experienced a slow exhumation history. During the 80–60 Ma, the fault system including TSPF, ZTMF, and YBQF from south to north underwent tectonic activity simultaneously (Figure 4), resulting in differential exhumation between blocks. Subsequently, the enhanced activity of TSPF controlled the uplift of Taishan Mountain, causing the rapid exhumation of the footwall at ~55 to 50 Ma.

4. Discussion

4.1. Interpretation of AHe Age Dispersion. Several samples show dispersion in single-grain ages that far exceeded the analytical error (Table 1 and Figure 3). Generally, several main factors can affect the dispersion of single-grain ages, such as the fragmentation effect [48], U/Th-rich inclusions [49, 50], eU content [44], grain size [51, 52], Ft correction [53, 54], ^{4}He implantation [55], and cooling rate [50]. Accordingly, we rule out the effect of fragmentation because all apatite grains analyzed in this study were almost intact (online Supplementary Figure S4). In the following, we focus on the remaining factors.

For apatite, the presence of U/Th-rich inclusions in grains can seriously affect AHe ages, generating old and/or anomalous ages [50]. However, no inclusions were detected in apatite crystals when we selected grains carefully using the high-power optical microscope, so we will not consider this further as the main reason for scattering ages. Similarly, variable eU content causes widely dispersed AHe ages, which can be used as a proxy for accumulated radiation damage. The higher eU in apatite can produce greater radiation damage and older ages [44, 56]. Except for sample TS01, there is no notable correlation between eU and ages (Figures 3(b), 3(e), and 3(h)). For sample TS01, the single-grain ages show a negative connection with eU. In AHe dating system, however, increasing levels of radiation damage from alpha recoil impede He diffusion, resulting in a higher closure temperature [44, 57]. The influence of radiation damage can yield a positive relationship between AHe ages and eU below the threshold (60, 80 ppm) [58]. Therefore, the negative correlation of sample TS01 might be the consequence of lacking enough grains. Previous studies also suggested that crystal grain sizes can affect the diffusion domain and closure temperature. The larger grains yield a higher closure temperature and older apparent ages [26, 51]. However, the ages of samples with dispersion (e.g., TS01, TS02, and TS04) do not show a clear correlation with equivalent sphere radius (Figures 3(c), 3(f), and 3(i)), demonstrating that grain sizes have little impact on ages. Furthermore, Ft correction is crucial for AHe dating [53]. When we correct, a homogeneous concentration distribution of U and Th is universally assumed because the distribution will in general be unknown. The corrected age will be overcorrected if the U and Th of the grain are at higher concentrations in the core. By contrast, the U and Th concentrations are rich in the rim, and the age will be smaller than the actual value. Farley [49] argued that typical corrections for minor accessory minerals between 0.65 and 0.9 would have the least uncertainty whereas Ft corrections of single grains are almost more than 0.65 (Table 1). Therefore, it indicates that the Ft correction should be excluded. Although a previous study has shown that ^{4}He implantation from the outside can cause older ages [55], Farley [49] and Wang et al. [59] suggest that ^{4}He implantation is irrelevant. However, we cannot assess whether it can affect the dating results in this study. In general, when the grains cooled rapidly, the variation of ages will be minimal. On the contrary, the sample cooled slowly or prolonged residence time in a partial retention zone before late burial heating, and the change of single-grain age can be considerable [7, 50, 60]. Such a scenario may provide a better explanation for the old ages in our study (online Supplementary Figure S2). Based on the above discussion, we consider that the cooling rate can have a crucial impact on the ages.

4.2. Fault Kinematic Characteristics

4.2.1. Spatiotemporal Variation across Taishan Extensional Fault System. The Taishan Mountain is made up of a succession of normal faults; as a result, its tectonic and geomorphological evolution is linked to the movement along these faults. The preservation of a sharp discontinuity in AHe ages across the fault system is indicative of differential fault movement [61]. To document the spatial evolution of the Taishan fault system, we integrated our AHe data with previously published AFT data available in two of the transects (Transects B and C, Figure 6).

Transect B displays only a modest difference in relief, with an elevation change of ~200 m across the length of the profile (Figures 2 and 3). Similarly, the AHe ages display modest variation in single-grain ages, increasing from 66 to 52 Ma in the footwall of YBQF to >70 Ma in the hanging wall. To the east, the AHe ages decrease to 58 Ma at 270 m in the footwall of ZTMF and then increase to 63 Ma with a lower elevation (240 m) in the footwall of TSPF or the hanging wall of the ZTMF. As all three normal faults strike parallel and dip in the same direction, we suggest that a single block is able to serve as both the footwall and the hanging wall of two faults (Figure 6(a)). Therefore, given the observation that the lowest elevation sample yielded the oldest age in this transect, we suggest that the region may have experienced northwestward, asymmetric tilting during fault activity [62–65].

A similar spatial pattern is observed in Transect C (Figure 6(b)). Although only four AFT data are presented in this transect, they record decreasing central ages with proximity to the YBQF. A similar distribution is preserved in the AHe data, where the AHe ages decrease from 74–70 to 68–65 Ma toward the YBQF. In the hanging wall of the YBQF, the AHe ages preserve a younging trend from 105 to 58–52 Ma closer to the ZTMF (Figure 6(b)). Moreover, the AHe ages climb significantly from the footwall to the hanging wall of the ZTMF, indicating differential cooling within the fault. The apparent ages between ZTMF and TSPF show a downward tendency at first, then begin to trend older toward the footwall of the TSPF, where the titling is the same as Transect B. Together, these AHe

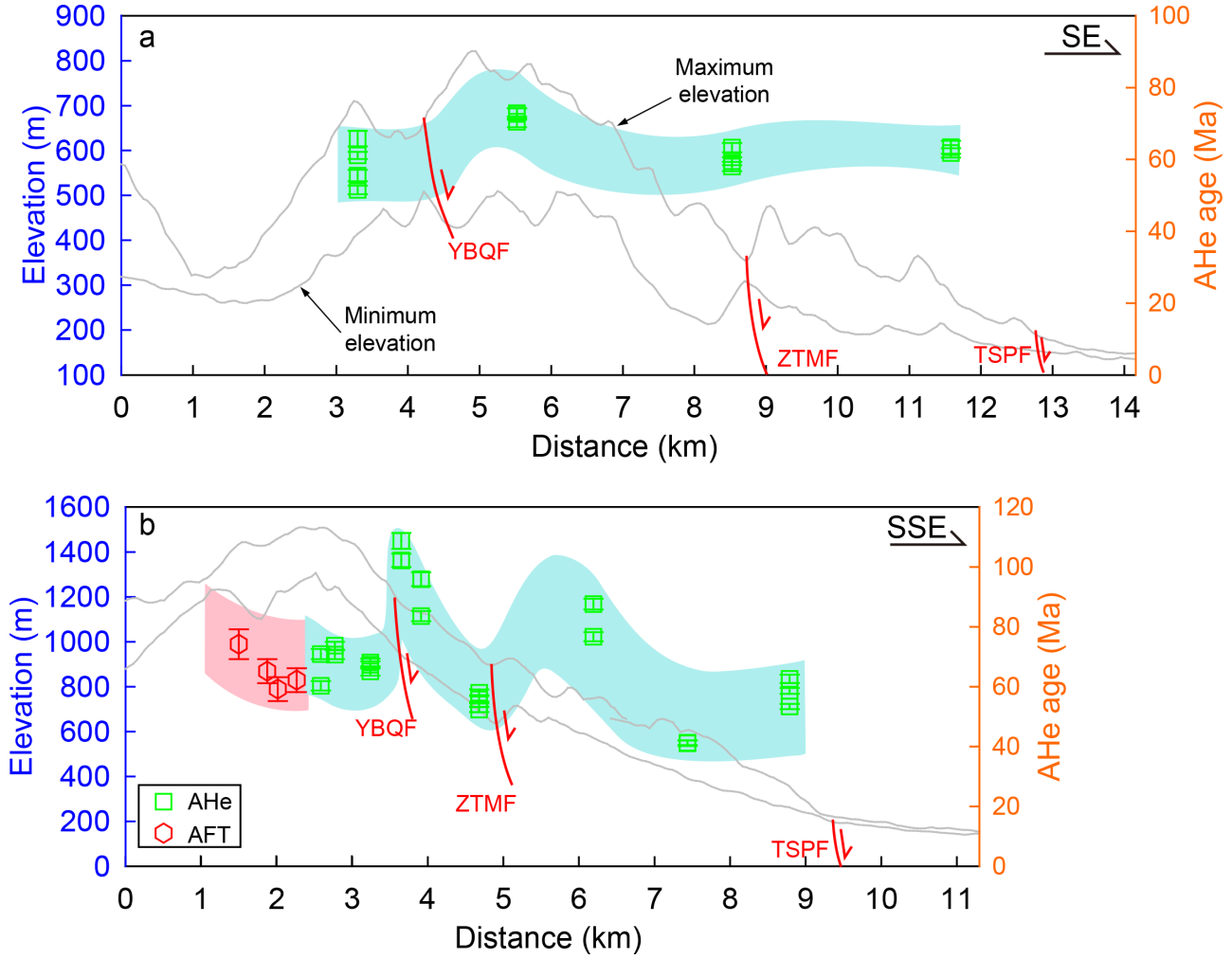

FIGURE 6: Projection of new AHe and published AFT data along the (a) Transect B and (b) Transect C. Topographic features were calculated using a 1 km circle window. The pink and pale turquoise areas envelope present apparent lateral differences in thermochronological ages through the YBQF, ZTMF, and TSPF. TSPF, Taishan Piedmont Fault; YBQF, Yunbuqiao Fault; ZTMF, Zhongtianmen Fault. The AFT data are derived from Tang [39].

data show systematic lateral differences over the transects, revealing fault-controlled differential cooling/exhumation across the Taishan.

In summary, low-temperature thermochronology is a powerful method for directly dating the cooling of rocks that accompany major normal fault slip in the upper crust during extension. When the fault slip is rapid and large enough to exhume samples from substantial depths to the surface, these thermochronological ages will constrain the timing of the extensional fault and range creation as well as the same record as thermal modeling [24, 66]. In general, the hanging wall of the normal fault moves downward along the fault relative to the footwall [22, 65]. Surprisingly, the individual models of all samples exhibit cooling episodes on both sides of faults (Figure 4). We infer that the TSPF may control the uplift of Taishan Mountain (Figure 2) [16]. In fact, our samples were taken from the footwall of TSPF (Figures 2 and 6), which began to uplift and was recorded by samples as the TSPF extended. If our hypothesis is correct, then why do the two walls of fault (e.g., YBQF) have different thermal histories captured by multisample models (Figure 5)? Generally, normal faults seldom occur as isolated features but within fault systems or populations (e.g., YBQF and ZTMF) [62, 63, 65]. Thus, these faults may be accompanied by the joint growth and interactions of differential tectonic activities to interpret such thermal histories as well as cause spatial variability in ages (Figures 2, 5, and 6) [4, 6, 67].

4.2.2. Spatial Exhumation Patterns across Taishan Extensional Fault System. To better constrain the spatial exhumation pattern, we estimated the long-term exhumation rates from AHe data, using the steady-state one-dimensional heat transport approach in Brandon et al. [68] and Reiners and Brandon [69]. Online Supplementary Table S1 lists the parameters required

for the calculating method, and the calculation results were implemented in self-compiling Python code (code is available from the author).

The exhumation rates calculated are displayed in Figure 7. Both transects have larger exhumation rates in the footwalls than in the hanging walls, indicating that both faults experienced significant dip sliding toward south-vergent normal faulting. Based on the AHe data, the rates of exhumation increased from <15 to >30 m/Myr from the hanging wall to the footwall. Previous studies have found that the Luxi Terrane preserves only a small magnitude of relief and thus, did not undergo intense tectonic movement until the Late Mesozoic [16]. As a result, we suggest that the differential exhumation rates across these faults (~15 m/Myr for YBQF and ZTMF) can be approximately quantified to estimate the long-term dip-slip rates. Unfortunately, as samples were not collected from the hanging wall of TSPF, differential exhumation rates across the TSPF could not be obtained. Given that AHe data suggest that the TSPF was responsible for Taishans exhumation, its rate must be greater than other faults (≥15 m/Myr). Finally, as all the fault dip angles are as high as 80°–85° [13, 14, 16], we estimate that the dip-slip rates are similar to the exhumation rates (i.e., ≥15 m/Myr).

4.3. Coupling Landscape Evolution with Normal Faulting in Taishan Mountain. Synthesizing thermal histories, fault kinematic characteristics, and geological analysis, we propose a four-stage model for deciphering the evolution of normal-fault bounded landscapes in response to the fault linkage processes of Taishan Mountain (Figure 8).

Starting in the mid-Cretaceous (100, 80 Ma), extension was initiated along three normal faults (YBQF, ZTMF, and TSPF) which exhumed the Taishan Mountain slowly due to the presence of a weaker tensional environment [70–72]. Although the extension allows the basin (hanging walls) to down-drop, the simultaneous uplift of the footwall is subdued [62] (Figure 8(a)). As a result, this may cause the fault system to unload relatively little material and not achieve the threshold of flexural rebound [73, 74].

In the Late Cretaceous (80, 60 Ma), the Taishan Mountain experienced accelerated exhumation and continued subsidence due to normal faulting (Figure 8(b)). We suggest that the TSPF, the YBQF, and the ZTMF underwent a period of enhanced extension forming the extensional tectonic setting (Figure 8(b)). The upper blocks of faults that have the shape of a downward tapered wedge will slide downward along fault planes. Whereas the flexural and isostatic rebound of the adjacent lower blocks produce uplift and form the tilted fault blocks northward to produce enhanced relief [62]. Following the extension, under the prolonged erosion, the overlying Cambrian–Ordovician sedimentary strata of uplift blocks were completely denuded, permitting the underlying metamorphic rocks to be exposed to the surface as recorded by the AHe data (Figure 3) [14, 16]. Based on the AHe data, we suggest that Taishan Mountain has been uplifted by ~1.2 km as constrained by the long-term dip-slip rate (~15 m/Myr) since the Late Cretaceous (80 Ma), which is consistent with the elevation difference between the Jade Emperor Peak and Tailai Basin [75]. Therefore, we propose that the Late Cretaceous episode of extension led to the formation of the proto-Taishan [13, 14, 16].

In the Early Cenozoic (60, 50 Ma), Taishan Mountain underwent a two-stage episode. The early episode (>55 Ma) is defined by slow exhumation and continued subsidence for different blocks of normal faults. However, after 55 Ma, the thermal history models suggest rapid cooling of fault blocks in the footwall of TSPF (Figure 8(c)). Both blocks of the ZTMF yielded a similar time of exhumation, which we interpret as a result of limited ZTMF activity relative to TSPF. In addition, although both blocks of the YBQF are uplifted, the cooling of its hanging wall is significantly older than its footwall. We suggest that the activity of YBQF may be relatively weak, and the block movement can be controlled by the TSPF. Previous studies have found that the Tailai Basin in the hanging wall of TSPF is filled with up to 2–3 km of Eocene clastic deposits (Guanzhuang Formation) [13, 14, 16]. Specifically, the bottom of the Guanshang Formation is dominated by the Paleozoic massive limestone breccias, which are considered as the product of rapid accumulation in the foothill [13, 14, 16]. Therefore, we can conclude that Taishan Mountain was uplifted and subjected to enhanced denudation controlled by the TSPF, which removed a large volume of material into the Tailai Basin during this period.

Finally, from the Early Cenozoic to the present (50, 0 Ma), the thermal history models are not well constrained by our AHe data and present a protracted quiescence or slight reheating (Figure 8(d)). In contrast, Liu et al. [76] utilized a linear inversion method to determine the spatial and temporal variation of exhumation rates in Luxi Terrane. They found that Taishan Mountain underwent an accelerating exhumation at 50–40 Ma, with a rate of 100 m/Myr. After which, Taishan Mountain experienced a substantial decrease in exhumation rates from 40 to 30 Ma and then increased from 30 to 20 Ma. Li et al. [19] integrated the AFT data and thermal history models and suggested that Taishan Mountain underwent two relatively enhanced exhumation events at 43–33 and 16–0 Ma. Furthermore, several previous studies also suggested that the Taishan Mountain is currently uplifting at a rate of 0.5 mm/y [13, 40], and active seismicities are frequently recorded [M6.5 in 1831 B.C. and M6.0 in 1668 A.D.] and triggered by the TSPF [38]. Together, these data suggest that Taishan Mountain underwent several tectonic uplifts since 50 Ma under an extensional regime which has formed the presently preserved tectonic edifice.

The modern relief is a function of the coupled evolution of climate and tectonics through time [28, 77, 78]. The Luxi Terrane including Taishan Mountain underwent the long-term arid and/or semiarid climate captured by the terrestrial deposits and numerical simulations between 100 and 24 Ma [79–82]. Prolonged aridity suppresses large surface erosion and can enhance rock uplift [83]. However, since the Miocene, the Luxi Terrane has been dominated by a humid climate that continues to the present day [80]. If the intense precipitation is the main force for

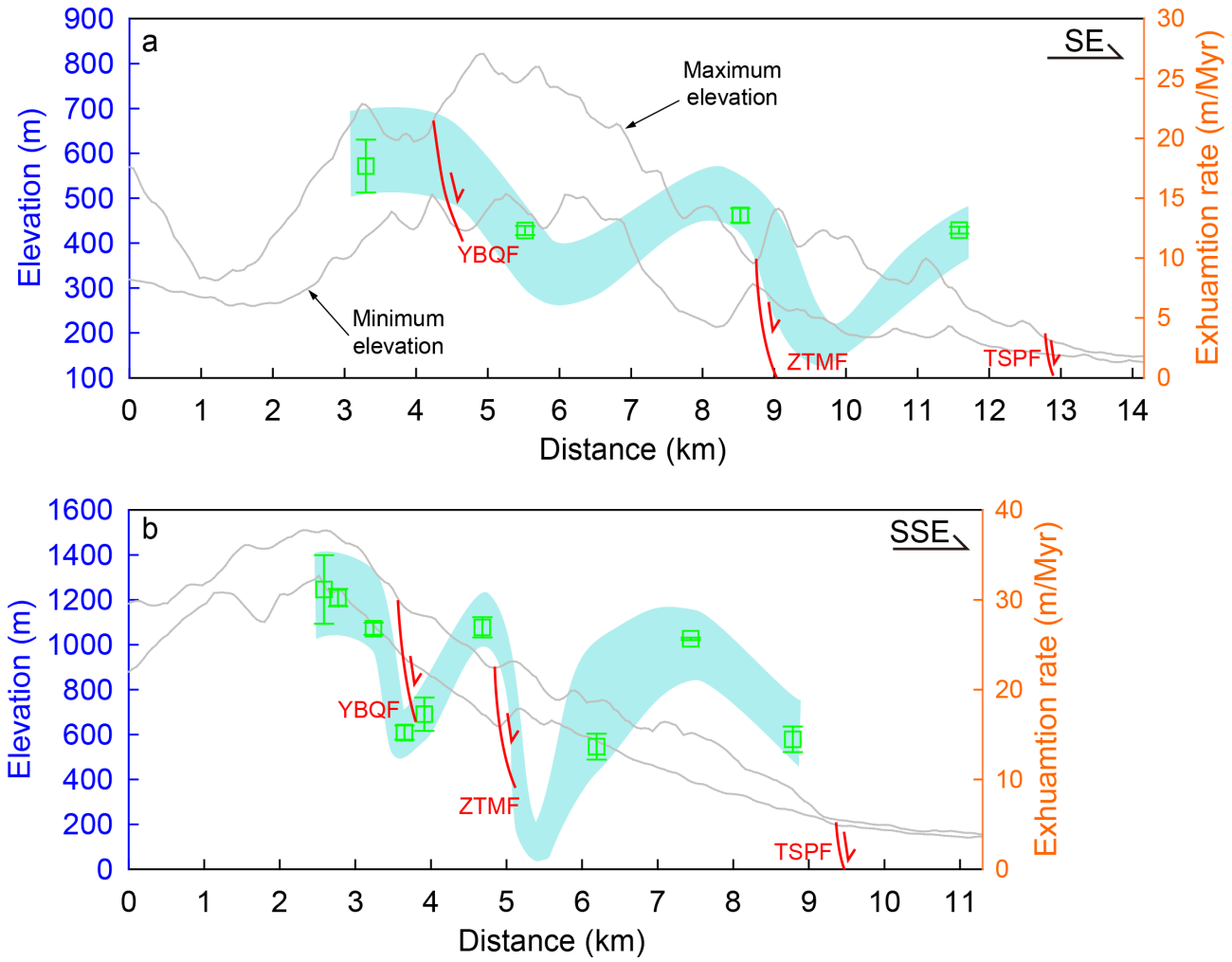

Figure 7: Spatial exhumation patterns across the (a) Transect B and (b) Transect C. The pale turquoise area envelopes all exhumation rates calculated from AHe ages. We do not consider AFT ages due to the lack of data on the hanging wall. This figure shows that average exhumation rates in the study area are strongly controlled by the normal fault system. TSPF, Taishan Piedmont Fault; YBQF, Yunbuqiao Fault; ZTMF, Zhongtianmen Fault.

surface erosion, the Luxi Terrane should produce widespread rapid exhumation events during Miocene. In the greater Luxi Terrane, however, only a few areas demonstrate rapid Miocene exhumation suggested by low-temperature thermochronology [76]. Thus, we suggest that normal faulting has played the dominant role in producing the observed landscape of Taishan Mountain.

4.4. Implications for Regional Geodynamics. Our thermal history modeling revealed that Taishan Mountain underwent two pulses of accelerated exhumation during the Late Cretaceous-Paleocene (80, 60 Ma) and Eocene (55, 50 Ma). We interpret the early cooling episode as the result of the growth and interactions of normal faults (YBQF, ZTMF, and TSPF), while the only enhanced activity of the TSPF controls the Eocene cooling. These findings raise the question of what drives the (re-)activation of these normal faults.

The Late Cretaceous-Paleocene rapid cooling signal is not only in Taishan but also in several neighboring tectonic units (e.g., Jiao Dong Peninsula, Dabie Mountains, Sulu Orogenic belt, and Trans-North China Orogen) [21, 84–87] and has even been documented in Korea and Japan [88–90]. There was an interesting pattern to the formation and evolution of these areas, with fault zones trending NNE or NE, including the Dabie, Jiao Dong, and Sulu along the Tan-Lu Fault Zone [84–87] and Ryoke and San'yo granites extension of SW Japan along the Median Tectonic Line [90]. Previous studies have elucidated that tectonic movements along the NNE- or NE-trending fault zones are closely linked to the movement orientations and subduction angles of the Izanagi Plate [71, 75, 91, 92]. Similarly, the ENE-oriented normal faults in Taishan Mountain, which are adjacent to the Tan-Lu Fault Zone (Figure 1), should be driven by the same mechanism, that is, the subduction of the Izanagi Plate.

To better identify the driving mechanism, we reconstructed the regional plate tectonics (Figure 9). As a result of the plate reconstruction, it was shown that the Izanagi Plate rotated counterclockwise during

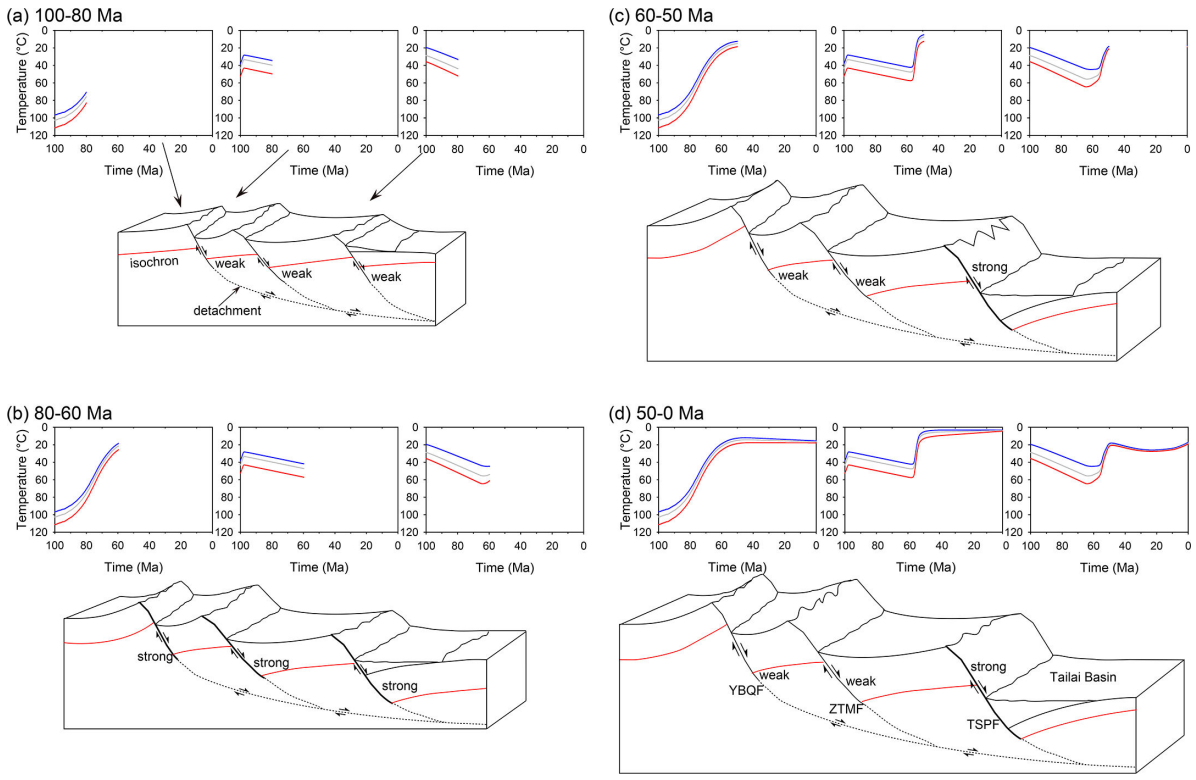

FIGURE 8: Conceptual model of the landscape evolution response to the normal faulting referred to the thermal history in Taishan Mountain since 100 Ma. TSPF, Taishan Piedmont Fault; YBQF, Yunbuqiao Fault; ZTMF, Zhongtianmen Fault.

the Late Cretaceous-Paleocene. Meanwhile, there was an alteration in the Izanagi Plate's motion rates from a strike-slip pattern to high-velocity orthogonal subduction beneath the Eurasian Plate [92]. Since 100 Ma (Figure 9(a)), it has been moving westward at a moderate rate (15 cm/y), then abruptly increased to ~23 cm/y at 80 Ma (Figure 9(b)), following decreased to ~4 to 6 cm/y until 60 Ma (Figure 9(c)). Decreased convergence rates may have reduced plate coupling and caused the plate to transition from a flat-slab to steep subduction with the retreat of the slab [93–95]. As a result of the slab retreat, the lithospheric thickness peaked in the Late Cretaceous-Paleogene at around 60 km and it caused widespread extension on the eastern margin of Eurasia [96–99]. In particular, the Gyeongsang Basin of the Korean Peninsula subsided as a back-arc basin in the Cretaceous owing to the slab rollback of the Izanagi Plate (Figure 1(a)) [91, 100, 101], undergoing intense W-E extension accompanied with the deposition of ~3 km thick terrestrial sediments [91, 101]. Furthermore, Liu et al. [102] investigated the structure of the mantle using a regional P-wave velocity tomography model. They found a big-mantle wedge beneath the Eurasian Plate, with the upper boundary of the subducting slab near the Daxing'anling-Taihangshan Gravity Lineament (Figure 1(a)) at the Late Cretaceous. To the east of Taishan Mountain, South Korea, Japan, and the southeastern coast of China preserved the vast Late Cretaceous igneous rock with the age eastward younging, corresponding to the retreat of the Izanagi slab [103, 104]. Consistency in the timing of tectonic activities and the fact that Taishan Mountain is positioned inside a slab activity zone suggest that the big-mantle wedge driven by the Izanagi slab subduction generated intense mantle flow convection and forced the Late Cretaceous-Paleocene extensional deformation of the YBQF, ZTMF, and TSPF [95]. In addition, Hu et al. [36] used the finite element approach to simulate the tectonic evolution of the entire Luxi Terrane between the Late Mesozoic and Paleogene. They discovered that only a real movement model of the Izanagi Plate can reconstruct the tectonic pattern of Luxi Terrane, implying that subduction of the Izanagi Plate contributed force to the tectonic deformation of Luxi Terrane.

The Early Cenozoic tectonics inherited the Mesozoic tectonic pattern. The Eocene fast cooling events can also be found in the same areas (e.g., Sulu orogenic belt, Dabie orogenic belt, Jiaodong Peninsula, Shanxi Rift, and Taihangshan region) [76]. The far-field consequence of the India–Eurasia collision [105–107] and the subduction of the Pacific Plate [8, 11] are considered as the two competing factors for triggering the rapid exhumation and extension at the Eocene. Based on the plate reconstruction models, the Indian Plate in the Eocene was close to the lower latitude region (Figure 9(c)), far away from the current Tibetan Plateau. It has been suggested that the Eocene collision took place as a result of a "soft" collision between the Tibetan-Himalayan microcontinent and Asia, and the

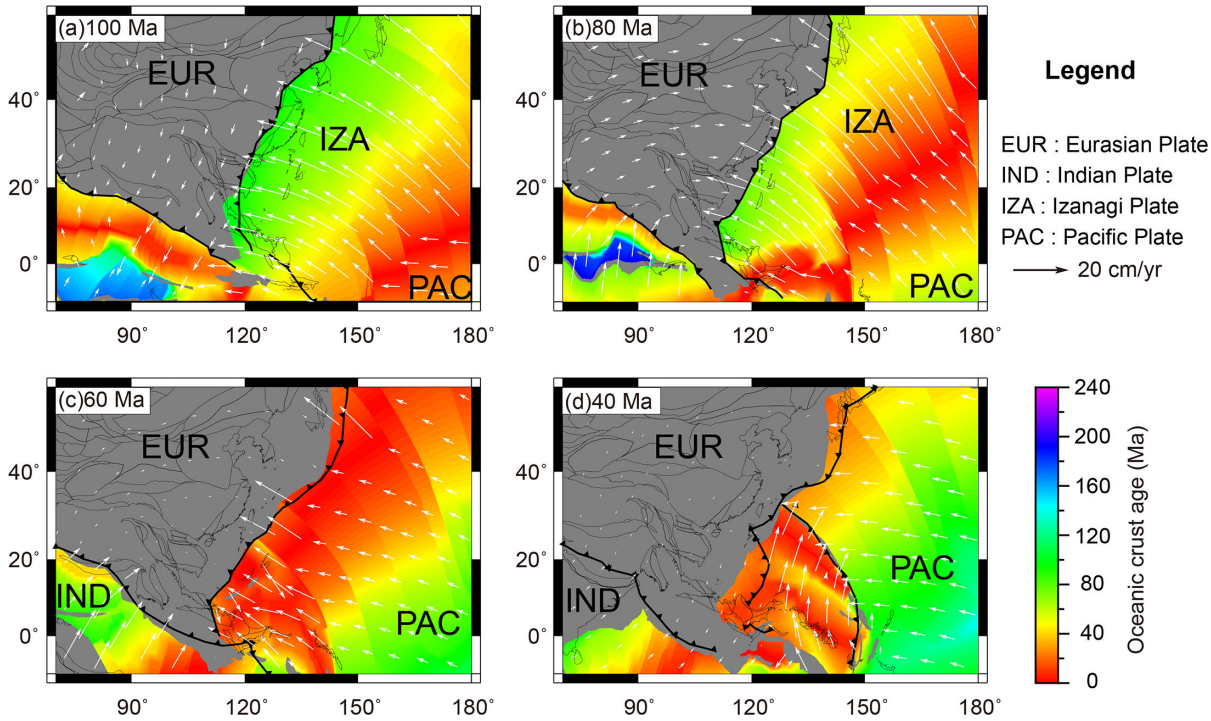

FIGURE 9: Plate reconstructions since 100 Ma, which show the age-area distribution of oceanic crust (colorful areas) at the time of formation, the absolute plate motion (white arrows), and the tectonic evolution (gray lines) of East Asia (modified from Müller et al. [134]). The black-toothed lines represent the subduction zone.

"hard" collision did not take place until 25 Ma or later according to Van Hinsbergen et al. [108] and Xiao et al. [109]. This collision event caused the upper crustal shortening and thickening in Asia, which corresponded to the Cenozoic deformation of the Asian continent [110–112]. Therefore, the far-field effect of Indian subduction beneath Eurasian may not be the major driving force, only as a limited tectonic response to the evolution of the eastern NCC.

We suggest that the main driver of cooling via tectonic exhumation in Taishan Mountain is a result of the subduction and slab retreat of the Pacific Plate. After 60 Ma, the Izanagi Plate was almost completely subducted beneath Eurasia Plate, and then the Pacific Plate replaced it with a subparallel subduct beneath Eurasia Plate (Figure 9(c)) [113]. Under this context, the Pacific Plate continued to move westward with a significant decrease in the convergence rate [92, 114]. Reduction of the convergence rate may be associated with a net decrease in horizontal compressional stress transmitted between the Pacific and Eurasian plates, leading to a period of widespread extension and normal faulting along the eastern margin of Eurasia than before (Figure 1) [114]. This scenario is very similar to that of the Basin and Range Province of the North American Cordillera [115, 116]. Previous studies have indicated that the Taihang-Lvliangshan controlled by normal fault underwent a rapid cooling during the Eocene based on low-temperature thermochronological data, with a high exhumation rate of 150–160 m/Myr [21, 84, 117–120]. They speculated this episode of rapid exhumation was closely associated with the depositional history of the western Bohai Bay Basin to the east (Figure 1(a)). By using the same technique, our new data and Li et al. [19] clarified that Taishan Mountain underwent an Eocene uplift, coupling with the subsidence of the Jiyang Depression (southern Bohai Bay Basin; Figure 1). The Jiyang Depression and Luxi Terrane (e.g., Taishan Mountain) share the same crystalline basement of Taishan Association [121]. However, their tectonic evolutions differentiated significantly since the Cenozoic [122]. The basement of the Jiyang Depression underwent substantial extensional faulting during the Paleogene, which resulted in the formation of ~1.8 km thick lacustrine deposits of sand and mudstone [121, 123]. In contrast, the Luxi Terrane underwent a continuous process of uplift and exhumation [76, 122]. Li et al. [124] examined the Kongdian Formation ($E_{1\text{-}2}k$) and Sha-4 Member (E_2s^4) of the Jiyang Depression and discovered numerous detrital high-pressure metamorphic minerals, such as glaucophane, barroisite, and phengite. They suggest that these provenances might be sourced from the Sulu orogenic belt or the adjacent Luxi Terrane (recycled deposits). This conclusion was further reinforced by Shi et al. [125]. In addition, the correspondence between the rates of subsidence in the basin and uplift in the mountains demonstrates a robust link between these processes, indicating that at least since the Cenozoic, the Jiyang Depression and Taishan Mountain have operated as a unified system [18, 122, 126]. Whereas the Bohai Bay Basin is bounded by NNE-striking normal and dextral faults at the eastern and western margins and E-W-trending normal faults at the northern and southern margins [127], the formation and development of which have been ascribed to the trench

retreat and ridge subduction along the western Pacific [128–130]. Furthermore, the sinistral motion of the Tanlu Fault ceased at ~55 Ma, followed by beginning dextral strike-slip motion [29, 83], which played a key role in the tectonic stress field, shifting from NS to NW-SE trending due to the counterclockwise rotation of subduction of the Pacific Plate (Figure 9(d)). This resulted in NE/ENE-oriented faults being widely developed than before, and convex-to-the-north extensional tectonic patterns were observed throughout the Luxi Terrane [36]. The rapid uplift of Taishan Mountain should be a closer relationship with this extensional setting.

5. Conclusions

Our new low-temperature thermochronological data in this study provide new constraints on the Meso-Cenozoic landscape evolution of the Taishan Mountain, eastern China. The single-grain AHe ages range from 113 to 30 Ma, which indicates a slow and protracted cooling history. Furthermore, the dispersion of AHe ages within intrasample results from the differentiated cooling rate during different stages. AHe ages and corresponding thermal modeling indicate two episodes of rapid exhumation between Late Cretaceous (~80 to 60 Ma) and Early Cenozoic (~55 to 50 Ma) at the Taishan Mountain, which are correlated with differential activities of normal faults. The one-dimensional modeling of exhumation determined the average long-term dip-slip rate of at least ~15 m/Myr among the normal fault systems (YBQF, ZTMF, and TSPF) in the Taishan Mountain.

During 100–80 Ma, the whole Taishan Mountain commenced a continuous, slow exhumation under a weaker tensional environment. Afterward (~80 to 60 Ma), Taishan Mountain began to accelerate uplift in response to the growth and interactions of normal faults (YBQF, ZTMF, and TSPF), which further promoted the formation of the prototype of the Taishan Mountain. Eventually, the intense activity of the TSPF alone controls the third-stage cooling/uplift (~55 to 50 Ma) and may be continued to the present day (last stage). The normal faulting of the Taishan Mountain is interpreted as tectonic responses to the lithospheric thinning resulting from the subduction of Izanagi-Pacific. Whereas, the climate change and the far-field effect of India's subduction beneath Eurasia might provide limited contributions to the landscape evolution of the final Taishan shape and the evolution of the eastern NCC.

Data Availability

All the data supporting the results of this study have been presented in the paper.

Conflicts of Interest

The authors declare no conflicts of interest.

Acknowledgments

The editors and two anonymous reviewers are thanked for their constructive comments to greatly improve this paper. We also thank Prof. Junsheng Nie and Dr. Yuqi Hao for their valuable discussion during the early version of this paper and Ms. Pu Li for her help regarding to sample collection in the field.

This work was jointly supported by the Earthquake Science and Technology Spark of the China Earthquake Administration (XH20034Y), the National Natural Science Foundation of China (42202077), the Natural Science Foundation of Gansu Province (22JR5RA440), the Horizontal Foundation of the Qilu Normal University (2021HX002), and the Guiding Special Funds of "Double First-Class (First-Class University and First-Class Disciplines)" (Grant No. 561119201) of Lanzhou University, China.

Supplementary Materials

Text S1: Apatite (U-Th)/He experimental procedures. Figure S1: Measured (U-Th)/He age plots of the Durango apatite. Figure S2: Thermal history models calculated by the QTQt for each apatite grain used for AHe dating. Figure S3: Thermal history models of samples TS12 and TS13 calculated by the QTQt. Figure S4: Images of apatite crystal grains from some samples. Table S1: Summary of the parameters used in the one-dimensional heat transport approach (Supplementary Material).

References

[1] G. A. Davis, B. J. Darby, Z. Yadong, and T. L. Spell, "Geometric and temporal evolution of an extensional detachment fault, Hohhot metamorphic core complex, inner Mongolia, China," *Geology*, vol. 30, no. 11, 2002.

[2] W. Lin, M. Faure, P. Monié, U. Schärer, and D. Panis, "Mesozoic extensional tectonics in eastern Asia: the south Liaodong Peninsula metamorphic core complex (NE China)," *The Journal of Geology*, vol. 116, no. 2, pp. 134–154, 2008.

[3] G. Zhu, Y. Chen, D. Jiang, and S. Lin, "Rapid change from compression to extension in the north China Craton during the early Cretaceous: evidence from the Yunmengshan metamorphic core complex," *Tectonophysics*, vol. 656, pp. 91–110, 2015.

[4] O. B. Duffy, S. H. Brocklehurst, R. L. Gawthorpe, M. R. Leeder, and E. Finch, "Controls on landscape and drainage evolution in regions of distributed normal faulting: Perachora Peninsula, Corinth rift, central Greece," *Basin Research*, vol. 27, no. 4, pp. 473–494, 2015.

[5] C. Heineke, R. Hetzel, N.-P. Nilius, et al., "Spatial patterns of erosion and landscape evolution in a bivergent metamorphic core complex revealed by cosmogenic ^{10}Be: the central Menderes Massif (western Turkey)," *Geosphere*, vol. 15, no. 6, pp. 1846–1868, 2019.

[6] D. C. Roda-Boluda and A. C. Whittaker, "Normal fault evolution and coupled landscape response: examples from

the southern Apennines, Italy," *Basin Research*, vol. 30, no. S1, pp. 186–209, 2018.

[7] C. Clinkscales, P. Kapp, and H. Wang, "Exhumation history of the north-central Shanxi rift, north China, revealed by low-temperature thermochronology," *Earth and Planetary Science Letters*, vol. 536, 2020.

[8] L. Huang and C. Liu, "Evolutionary characteristics of the sags to the east of Tan–Lu fault zone, Bohai Bay basin (China): implications for hydrocarbon exploration and regional tectonic evolution," *Journal of Asian Earth Sciences*, vol. 79, no. Part A, pp. 275–287, 2014.

[9] S. Li, Y. Suo, L. Dai, et al, "Development of the Bohai Bay basin and destruction of the north China craton," *Earth Science Frontiers*, vol. 17, no. 4, pp. 64–89, 2010.

[10] L. Li, D. Zhong, C. Yang, et al, "Extension order and its deep geological background: evidence from western Shandong rise and Jiyang depression in the late Mesozoic-Cenozoic," *Earth Science Frontiers*, vol. 19, no. 5, pp. 255–273, 2012.

[11] P. Su, H. He, X. Tan, Y. Liu, F. Shi, and E. Kirby, "Initiation and evolution of the Shanxi rift system in north China: evidence from low-temperature thermochronology in a plate reconstruction framework," *Tectonics*, vol. 40, no. 3, 2021.

[12] G. Wang, S. Li, Z. Wu, et al, "Early paleogene strike-slip transition of the Tan–Lu fault zone across the southeast Bohai Bay basin: constraints from fault characteristics in its adjacent basins," *Geological Journal*, vol. 54, no. 2, pp. 835–849, 2019.

[13] P. Lv, M. Zhang, and Y. Zhang, "Formation of recent Mount Tai and geomorphologic landscapes are concerned with neotectonism," *Journal of Shandong Mining Institute*, vol. 14, no. 4, pp. 331–335, 1995.

[14] M. Zhang, Z. Jin, P. Lv, and G. Liu, "Formation of Taishan mountain and cenozoic tectonicism," *Journal of Geomechanics*, vol. 6, no. 2, pp. 23–29, 2000.

[15] S. Yan, G. Wang, Z. Shao, and X. Meng, "Extension model of crust uplifting in western Shandong," *Acta Geologica Sinica - English Edition*, vol. 9, no. 3, pp. 219–232, 1996.

[16] P. Lv, "The formation of the Taishan and its age," *Journal of Shandong Mining Institute*, no. 2, pp. 14–19, 1984.

[17] L. Li and D. Zhong, "Fission track evidence of cenozoic uplifting events of the Taishan, China," *Acta Petrologica Sinica*, vol. 22, no. 2, pp. 457–464, 2006.

[18] L. Li, D. Zhong, and X. Shi, "Cenozoic uplifting/subsidence coupling between the west Shandong rise and the Jiyang depression, northern China," *Acta Geologica Sinica*, vol. 81, no. 9, pp. 1215–1228, 2007.

[19] L. Li, D. Zhong, C. Yang, X. Shi, L. Zhao, and D. Dong, "The coupling relationship between the west Shandong rise and the Jiyang depression, China," *Journal of Earth Science*, vol. 24, no. 4, pp. 626–644, 2013.

[20] P. F. Green, I. R. Duddy, A. J. W. Gleadow, P. R. Tingate, and G. M. Laslett, "Thermal annealing of fission tracks in apatite: 1. A qualitative description," *Chemical Geology: Isotope Geoscience Section*, vol. 59, pp. 237–253, 1986.

[21] C. Clinkscales, P. Kapp, S. Thomson, et al., "Regional exhumation and tectonic history of the Shanxi rift and Taihangshan, north China," *Tectonics*, vol. 40, no. 3, 2021.

[22] T. A. Ehlers, P. A. Armstrong, and D. S. Chapman, "Normal fault thermal regimes and the interpretation of low-temperature thermochronometers," *Physics of the Earth and Planetary Interiors*, vol. 126, nos. 3–4, pp. 179–194, 2001.

[23] S. A. Johnstone and J. P. Colgan, "Interpretation of low-temperature thermochronometer ages from tilted normal fault blocks," *Tectonics*, vol. 37, no. 10, pp. 3647–3667, 2018.

[24] D. F. Stockli, B. E. Surpless, T. A. Dumitru, and K. A. Farley, "Thermochronological constraints on the timing and magnitude of Miocene and Pliocene extension in the central Wassuk range, western Nevada," *Tectonics*, vol. 21, no. 4, pp. 10–11, 2002.

[25] W. Zhang, F. Wang, L. Wu, et al., "Reactivated margin of the western north China Craton in the late Cretaceous: constraints from Zircon (U-Th)/He thermochronology of Taibai mountain," *Tectonics*, vol. 41, no. 2, 2022.

[26] K. A. Farley, "Helium diffusion from apatite: general behavior as illustrated by Durango fluorapatite," *Journal of Geophysical Research*, vol. 105, no. B2, pp. 2903–2914, 2000.

[27] R. A. Wolf, K. A. Farley, and L. T. Silver, "Helium diffusion and low-temperature thermochronometry of apatite," *Geochimica et Cosmochimica Acta*, vol. 60, no. 21, pp. 4231–4240, 1996.

[28] F. Liu, M. Danišík, D. Zheng, K. Gallagher, and J. Nie, "Distinguishing tectonic versus climatic forcing on landscape evolution: an example from SE Tibetan plateau," *GSA Bulletin*, vol. 133, nos. 1–2, pp. 233–242, 2021.

[29] F. Yang, G. Jepson, C. Liu, et al., "Uplift-exhumation and preservation of the Yumugou Mo-W deposit, east Qinling, China: insights from multiple apatite low-temperature thermochronology," *Ore Geology Reviews*, vol. 141, p. 104670, 2022.

[30] B. M. Jahn, B. Auvray, Q. H. Shen, et al., "Archean crustal evolution in China: the Taishan complex, and evidence for juvenile crustal addition from long-term depleted mantle," *Precambrian Research*, vol. 38, no. 4, pp. 381–403, 1988.

[31] T. Peng, S. A. Wilde, W. Fan, and B. Peng, "Late Neoarchean potassic high Ba-Sr granites in the Taishan granite-greenstone terrane: petrogenesis and implications for continental crustal evolution," *Chemical Geology*, vol. 344, pp. 23–41, 2013.

[32] Y. Chen, J. Zhang, J. Liu, et al., "Crustal growth and reworking of the eastern north China craton: constraints from the age and geochemistry of the Neoarchean Taishan TTG Gneisses," *Precambrian Research*, vol. 343, 2020.

[33] G. Cao, *Early precambrian geology of western Shandong*, Geological Publishing House, Beijing, China, 1996.

[34] Y. Wan, D. Liu, S. Wang, et al., "~2.7 Ga juvenile crust formation in the north China Craton (Taishan-Xintai area, western Shandong province): further evidence of an understated event from U-Pb dating and Hf isotopic composition of zircon," *Precambrian Research*, vol. 186, nos. 1–4, pp. 169–180, 2011.

[35] W. Wang, E. Yang, M. Zhai et al., "Geochemistry of 2.7 Ga basalts from Taishan area: constraints on the evolution of early Neoarchean granite-greenstone belt in western Shandong Province, China," Precambrian Research, vol. 224, pp. 94–109, 2013.

[36] Q. Hu, L. Li, and J. Guo, "The late Mesozoic-Paleoproterozoic tectonic evolution and numerical simulation between the Luxi uplift and Jiyang depression," *Journal of Shengli*

College China University of Petroleum, vol. 32, no. 1, pp. 1–7, 2018.

[37] P. Lv and X. Zhu, "Changes of tectonic stress fields of Mesozoic and Cenozoic eras in western Shandong," *Journal of Shandong Mining Institute*, vol. 8, no. 4, pp. 18–25, 1989.

[38] H. Chao, Z. Wang, J. Li, and Z. Gui, "The latest activities of faults in the Tai'an region, Shandong province and the Taishan mountain earthquake," *Seismology and Geology*, vol. 21, no. 2, pp. 105–114, 1999.

[39] Z. Tang, "The Cenozoic uplifting-subsiding relation between Luxi uplift and Jiyang depression (Master thesis)," China University of Petroleum, Qingdao, 2010.

[40] P. Lv, D. Mo, F. Yang, J. Wang, and J. Niu, "Geo-science value of mount Taishan and its significance," *Journal of Shandong University of Science and Technology (Natural Science*), vol. 22, no. 2, pp. 33–36, 2003.

[41] J. Yu, D. Zheng, J. Pang, et al., "Miocene range growth along the Altyn Tagh fault: insights from apatite fission track and (U-Th)/He thermochronometry in the western Danghenan shan, China," *Journal of Geophysical Research*, vol. 124, no. 8, pp. 9433–9453, 2019.

[42] F. W. McDowell, W. C. McIntosh, and K. A. Farley, "A precise ^{40}Ar-^{39}Ar reference age for the Durango apatite (U-Th)/He and fission-track dating standard," *Chemical Geology*, vol. 214, nos. 3–4, pp. 249–263, 2005.

[43] K. Gallagher, "Transdimensional inverse thermal history modeling for quantitative thermochronology," *Journal of Geophysical Research*, vol. 117, no. B2, 2012.

[44] R. M. Flowers, R. A. Ketcham, D. L. Shuster, and K. A. Farley, "Apatite (U-Th)/He thermochronometry using a radiation damage accumulation and annealing model," *Geochimica et Cosmochimica Acta*, vol. 73, no. 8, pp. 2347–2365, 2009.

[45] L. Gourbet, R. Yang, M. G. Fellin, et al., "Evolution of the Yangtze river network, southeastern Tibet: insights from thermochronology and sedimentology," *Lithosphere*, vol. 12, no. 1, pp. 3–18, 2020.

[46] K. Gallagher, "Comment on "Thermal history modelling: HeFTy vs. QTQt" by Vermeesch and Tian," *Earth-Science Reviews,*, vol. 176, pp. 387–394, 2018.

[47] A. L. Abbey, M. Wildman, A. L. Stevens Goddard, and K. E. Murray, "Thermal history modeling techniques and interpretation strategies: applications using QTQt," *Geosphere*, vol. 19, no. 2, pp. 493–530, 2023.

[48] R. W. Brown, R. Beucher, S. Roper, C. Persano, F. Stuart, and P. Fitzgerald, "Natural age dispersion arising from the analysis of broken crystals. part I: theoretical basis and implications for the apatite (U-Th)/He thermochronometer," *Geochimica et Cosmochimica Acta*, vol. 122, no. 3, pp. 478–497, 2013.

[49] K. A. Farley, "(U-Th)/He dating: techniques, calibrations, and applications," *Reviews in Mineralogy and Geochemistry*, vol. 47, no. 1, pp. 819–844, 2002.

[50] P. G. Fitzgerald, S. L. Baldwin, L. E. Webb, and P. B. O'Sullivan, "Interpretation of (U–Th)/He single grain ages from slowly cooled crustal terranes: a case study from the Transantarctic mountains of southern Victoria Land," *Chemical Geology*, vol. 225, nos. 1–2, pp. 91–120, 2006.

[51] M. A. House, B. P. Kohn, K. A. Farley, and A. Raza, "Evaluating thermal history models for the Otway basin, southeastern Australia, using (U-Th)/He and fission-track data from Borehole apatites," *Tectonophysics*, vol. 349, nos. 1–4, pp. 277–295, 2002.

[52] P. W. Reiners and K. A. Farley, "Influence of crystal size on Apatite (U-Th)/He thermochronology: an example from the Bighorn mountains, Wyoming," *Earth and Planetary Science Letters*, vol. 188, nos. 3–4, pp. 413–420, 2001.

[53] K. A. Farley, R. A. Wolf, and L. T. Silver, "The effects of long alpha-stopping distances on (U-Th)/He ages," *Geochimica et Cosmochimica Acta*, vol. 60, no. 21, pp. 4223–4229, 1996.

[54] A. G. C. A. Meesters and T. J. Dunai, "Solving the production-diffusion equation for finite diffusion domains of various shapes," *Chemical Geology*, vol. 186, nos. 3–4, 2002.

[55] C. Spiegel, B. Kohn, D. Belton, Z. Berner, and A. Gleadow, "Apatite (U-th-Sm)/He thermochronology of rapidly cooled samples: the effect of he implantation," *Earth and Planetary Science Letters*, vol. 285, nos. 1–2, pp. 105–114, 2009.

[56] R. M. Flowers, D. L. Shuster, B. P. Wernicke, and K. A. Farley, "Radiation damage control on apatite (U-Th)/He dates from the grand Canyon region, Colorado plateau," *Geology*, vol. 35, no. 5, 2007.

[57] C. Gautheron, L. Tassan-Got, J. Barbarand, and M. Pagel, "Effect of alpha-damage annealing on apatite (U-Th)/He thermochronology," *Chemical Geology*, vol. 266, nos. 3–4, pp. 157–170, 2009.

[58] A. Recanati, C. Gautheron, J. Barbarand, et al., "Helium trapping in apatite damage: insights from (U-Th-Sm)/He dating of different granitoid lithologies," *Chemical Geology*, vol. 470, pp. 116–131, 2017.

[59] Y. Wang, F. Wang, L. Wu, W. Shi, and L. Yang, "U-Th)/He thermochronology of metallic ore deposits in the Liaodong Peninsula: implications for Orefield evolution in northeast China," *Ore Geology Reviews*, vol. 92, pp. 348–365, 2018.

[60] M. Fox and D. L. Shuster, "The influence of burial heating on the (U-Th)/He system in apatite: grand canyon case study," *Earth and Planetary Science Letters*, vol. 397, pp. 174–183, 2014.

[61] R. O. Lease and T. A. Ehlers, "Incision into the eastern Andean plateau during Pliocene cooling," *Science*, vol. 341, no. 6147, pp. 774–776, 2013.

[62] J. A. DiPietro, "Normal Fault-Dominated Landscapes," Elsevier, 2013.

[63] J. A. Jackson, N. J. White, Z. Garfunkel, and H. Anderson, "Relations between normal-fault geometry, tilting and vertical motions in extensional terrains: an example from the southern Gulf of Suez," *Journal of Structural Geology*, vol. 10, no. 2, pp. 155–170, 1988.

[64] D. McPhillips and M. T. Brandon, "Using tracer thermochronology to measure modern relief change in the Sierra Nevada, California," *Earth and Planetary Science Letters*, vol. 296, nos. 3–4, pp. 373–383, 2010.

[65] D. F. Stockli, K. A. Farley, and T. A. Dumitru, "Calibration of the apatite (U-Th)/He thermochronometer on an exhumed fault block, White mountains, California," *Geology*, vol. 28, no. 11, pp. 983–986, 2000.

[66] T. A. Ehlers and K. A. Farley, "Apatite (U–Th)/He thermochronometry: methods and applications to problems in tectonic and surface processes," *Earth and Planetary Science Letters*, vol. 206, nos. 1–2, pp. 1–14, 2003.

[67] P. A. Cowie, M. Attal, G. E. Tucker, et al, "Investigating the surface process response to fault interaction and linkage using a numerical modelling approach," *Basin Research*, vol. 18, no. 3, pp. 231–266, 2006.

[68] M. T. Brandon, M. K. Roden-Tice, and J. I. Garver, "Late Cenozoic exhumation of the Cascadia accretionary wedge in the Olympic Mountains, northwest Washington State," Geological Society of America Bulletin, vol. 110, no.8, pp. 617–630, 1998.

[69] P. W. Reiners and M. T. Brandon, "Using thermochronology to understand orogenic erosion," *Annual Review of Earth and Planetary Sciences*, vol. 34, no. 1, pp. 419–466, 2006.

[70] R. Zhu, H. Zhang, G. Zhu, et al., "Craton destruction and related resources," *International Journal of Earth Sciences*, vol. 106, no. 7, pp. 2233–2257, 2017.

[71] G. Zhu, C. Liu, C. Gu, et al., "Oceanic plate subduction history in the western Pacific ocean: constraint from late Mesozoic evolution of the Tan-Lu fault zone," *Science China Earth Sciences*, vol. 61, no. 4, pp. 386–405, 2018.

[72] R. Zhu and Y. Xu, "The subduction of the west Pacific plate and the destruction of the North China craton," *Science China Earth Sciences*, vol. 62, no. 9, pp. 1340–1350, 2019.

[73] S. S. Egan, "The flexural isostatic response of the lithosphere to extensional tectonics," *Tectonophysics*, vol. 202, nos. 2–4, pp. 291–308, 1992.

[74] B. Wernicke and G. J. Axen, "On the role of isostasy in the evolution of normal fault systems," *Geology*, vol. 16, no. 9, 1988.

[75] Y. Zhang, S. Dong, and W. Shi, "Cretaceous deformation history of the middle Tan-Lu fault zone in Shangdong province, eastern China," *Tectonophysics*, vol. 363, nos. 3–4, pp. 243–258, 2003.

[76] C. Liu, G. Li, and F. Liu, "Early Cretaceous-Cenozoic exhumation history of Luxi terrane and adjacent areas, eastern north China craton," *Geological Journal*, vol. 57, no. 7, pp. 2735–2748, 2022.

[77] A. Bahadori, W. E. Holt, R. Feng, et al., "Coupled influence of tectonics, climate, and surface processes on landscape evolution in southwestern north America," *Nature Communications*, vol. 13, no. 1, 2022.

[78] J. Nie, G. Ruetenik, K. Gallagher, et al., "Rapid Incision of the Mekong river in the middle miocene linked to monsoonal precipitation," *Nature Geoscience*, vol. 11, no. 12, pp. 944–948, 2018.

[79] A. Farnsworth, D. J. Lunt, S. A. Robinson, et al., "Past east Asian monsoon evolution controlled by paleogeography, not CO_2," *Science Advances*, vol. 5, no. 10, 2019.

[80] Z. T. Guo, B. Sun, Z. S. Zhang, et al., "A major reorganization of Asian climate by the early Miocene," *Climate of the Past*, vol. 4, no. 3, pp. 153–174, 2008.

[81] S. Li, S. E. Grasby, X. Zhao, et al., "Mercury evidence of deccan volcanism driving the latest Maastrichtian warming event," *Geology*, vol. 50, no. 10, pp. 1140–1144, 2022.

[82] D. Xi, X. Wan, G. Li, and G. Li, "Cretaceous integrative stratigraphy and timescale of China," *Science China Earth Sciences*, vol. 62, no. 1, pp. 256–286, 2019.

[83] E. R. Sobel, G. E. Hilley, and M. R. Strecker, "Formation of internally drained contractional basins by aridity-limited bedrock incision," *Journal of Geophysical Research: Solid Earth*, vol. 108, no. B7, p. 2344, 2003.

[84] J. Chang, N. Qiu, S. Liu, C. Cai, Q. Xu, and N. Liu, "Post-Triassic multiple exhumation of the Taihang mountains revealed via low-T thermochronology: implications for the paleo-geomorphologic reconstruction of the north China craton," *Gondwana Research*, vol. 68, pp. 34–49, 2019.

[85] Z. Liu, J. Wang, D. Zheng, et al, "Exploration prospect and postore denudation in the northwestern Jiaodong gold province, China: evidence from apatite fission track thermochronology," *Acta Petrologica Sinica*, vol. 26, pp. 3597–3611, 2010.

[86] F. Yang, M. Santosh, S. Glorie, G. Jepson, F. Xue, and S. W. Kim, "Meso-Cenozoic multiple exhumation in the Shandong Peninsula, eastern north China craton: implications for lithospheric destruction," *Lithos*, vols. 370–371, p. 105597, 2020.

[87] Z. H. U. Guang, H. O. U. Minjin, W. Yongsheng, L. I. U. Guosheng, and N. I. U. Manlan, "Thermal evolution of the Tanlu fault zone on the eastern margin of the Dabie mountains and its tectonic implications," *Acta Geologica Sinica - English Edition*, vol. 78, no. 4, pp. 940–953, 2004.

[88] H. Cho, M. Son, Y. Cheon, Y. K. Sohn, J.-S. Kim, and H.-C. Kang, "Evolution of the late cretaceous Dadaepo basin, SE Korea, in response to oblique subduction of the proto-Pacific (Izanagi/Kula) or Pacific plate," *Gondwana Research*, vol. 39, pp. 145–164, 2016.

[89] T. Choi and Y. I. Lee, "Thermal histories of cretaceous basins in Korea: implications for response of the east asian continental margin to subduction of the Paleo-Pacific plate," *Island Arc*, vol. 20, no. 3, pp. 371–385, 2011.

[90] O. Kinoshita, "Migration of igneous activities related to ridge subduction in southwest Japan and the east Asian continental margin from the Mesozoic to the Paleogene," *Tectonophysics*, vol. 245, nos. 1–2, pp. 25–35, 1995.

[91] S. K. Chough and Y. K. Sohn, "Tectonic and sedimentary evolution of a Cretaceous continental arc-backarc system in the Korean Peninsula: new view," *Earth-Science Reviews*, vol. 101, nos. 3–4, pp. 225–249, 2010.

[92] S. Maruyama, Y. Isozaki, G. Kimura, and M. Terabayashi, "Paleogeographic maps of the Japanese islands: plate tectonic synthesis from 750 Ma to the present," *Island Arc*, vol. 6, no. 1, pp. 121–142, 1997.

[93] J. C. Grimmer, R. Jonckheere, E. Enkelmann, et al., "Cretaceous-Cenozoic history of the Southern Tan-Lu fault zone: apatite fission-track and structural constraints from the Dabie shan (eastern China)," *Tectonophysics*, vol. 359, nos. 3–4, pp. 225–253, 2002.

[94] L. Liu, D. Peng, L. Liu, et al., "East Asian lithospheric evolution dictated by multistage Mesozoic flat-slab subduction," *Earth-Science Reviews*, vol. 217, p. 103621, 2021.

[95] X. Xu, A. V. Zuza, L. Chen, et al., "Late Cretaceous to early Cenozoic extension in the lower Yangtze region (East China) driven by Izanagi-Pacific plate subduction," *Earth-Science Reviews*, vol. 221, p. 103790, 2021.

[96] Y.-G. Xu, "Thermo-tectonic destruction of the Archaean lithospheric keel beneath the Sino-Korean Craton in China: evidence, timing and mechanism," *Physics and Chemistry of the Earth, Part A Solid Earth and Geodesy*, vol. 26, nos. 9–10, pp. 747–757, 2001.

[97] Y.-G. Xu, "Recycled Oceanic crust in the source of 90–40 Ma basalts in north and northeast China: evidence, provenance and significance," *Geochimica et Cosmochimica Acta*, vol. 143, pp. 49–67, 2014.

[98] Y. Xu, H. Li, C. Pang, and B. He, "On the timing and duration of the destruction of the north China Craton," *Science Bulletin*, vol. 54, no. 19, pp. 3379–3396, 2009.

[99] F. Yang, M. Santosh, S. W. Kim, H. Zhou, and Y. J. Jeong, "Late Mesozoic intraplate rhyolitic volcanism in the north China craton: far-field effect from the westward subduction of the Paleo-Pacific plate," *GSA Bulletin*, vol. 132, nos. 1–2, pp. 291–309, 2020.

[100] Y. Li, W.-L. Xu, R.-X. Zhu, F. Wang, W.-C. Ge, and A. A. Sorokin, "Late Jurassic to early early cretaceous tectonic nature on the NE Asian continental margin: constraints from Mesozoic accretionary complexes," *Earth-Science Reviews*, vol. 200, p. 103042, 2020.

[101] Y.-B. Zhang, M. Zhai, Q.-L. Hou, T.-S. Li, F. Liu, and B. Hu, "Late Cretaceous volcanic rocks and associated granites in Gyeongsang basin, SE Korea: their chronological ages and tectonic implications for Cratonic destruction of the north China Craton," *Journal of Asian Earth Sciences*, vol. 47, pp. 252–264, 2012.

[102] X. Liu, D. Zhao, S. Li, and W. Wei, "Age of the subducting pacific slab beneath east Asia and its Geodynamic implications," *Earth and Planetary Science Letters*, vol. 464, pp. 166–174, 2017.

[103] S. Li, Y. Suo, X. Li, et al., "Mesozoic tectono-magmatic response in the east Asian ocean-continent connection zone to subduction of the Paleo-Pacific plate," *Earth-Science Reviews*, vol. 192, pp. 91–137, 2019.

[104] G. Xing, R. Chen, Z. Yang, et al, "Characteristics and tectonic setting of late Cretaceous volcanic magmatism in the coastal southeast China," *Acta Petrologica Sinica*, vol. 25, pp. 77–91, 2009.

[105] M. Liu, X. Cui, and F. Liu, "Cenozoic rifting and volcanism in eastern China: a mantle dynamic link to the Indo-Asian collision?," *Tectonophysics*, vol. 393, nos. 1–4, pp. 29–42, 2004.

[106] P. Molnar and P. Tapponnier, "Relation of the tectonics of eastern China to the India- Eurasia collision: application of slip-line field theory to large-scale continental tectonics," *Geology*, vol. 5, no. 4, 1977.

[107] P. Tapponnier, G. Peltzer, A. Y. Le Dain, R. Armijo, and P. Cobbold, "Propagating extrusion tectonics in Asia: new insights from simple experiments with plasticine," *Geology*, vol. 10, no. 12, 1982.

[108] D. J. J. van Hinsbergen, P. C. Lippert, G. Dupont-Nivet, et al., "Greater India Basin hypothesis and a two-stage cenozoic collision between India and Asia," *Proceedings of the National Academy of Sciences of the United States of America*, vol. 109, no. 20, pp. 7659–7664, 2012.

[109] W. Xiao, S. Ao, L. Yang, et al., "Anatomy of composition and nature of plate convergence: insights for alter-native thoughts for terminal India-Eurasia collision," *Science China Earth Sciences*, vol. 60, no. 6, pp. 1015–1039, 2017.

[110] T. M. Harrison, P. Copeland, W. S. F. Kidd, and A. Yin, "Raising Tibet," *Science (New York, N.Y.)*, vol. 255, no. 5052, pp. 1663–1670, 1992.

[111] E. R. Sobel, J. Chen, and R. V. Heermance, "Late Oligocene-early Miocene initiation of shortening in the southwestern Chinese Tian shan: implications for Neogene shortening rate variations," *Earth and Planetary Science Letters*, vol. 247, nos. 1–2, pp. 70–81, 2006.

[112] A. Yin, "Cenozoic tectonic evolution of Asia: a preliminary synthesis," *Tectonophysics*, vol. 488, nos. 1–4, pp. 293–325, 2010.

[113] M. Seton, N. Flament, J. Whittaker, R. D. Müller, M. Gurnis, and D. J. Bower, "Ridge subduction sparked reorganization of the pacific plate-mantle system 60-50 million years ago," *Geophysical Research Letters*, vol. 42, no. 6, pp. 1732–1740, 2015.

[114] C. J. Northrup, L. H. Royden, and B. C. Burchfiel, "Motion of the Pacific plate relative to Eurasia and its potential relation to Cenozoic extension along the eastern margin of Eurasia," *Geology*, vol. 23, no. 8, 1995.

[115] W. R. Dickinson, "The basin and range province as a composite extensional domain," *International Geology Review*, vol. 44, no. 1, pp. 1–38, 2002.

[116] L. Le Pourhiet, M. Gurnis, and J. Saleeby, "Mantle instability beneath the Sierra Nevada mountains in California and death valley extension," *Earth and Planetary Science Letters*, vol. 251, nos. 1–2, pp. 104–119, 2006.

[117] X. Cao, S. Li, L. Xu, et al., "Mesozoic-Cenozoic evolution and mechanism of tectonic geomorphology in the central north China block: constraint from apatite fission track thermochronology," *Journal of Asian Earth Sciences*, vol. 114, pp. 41–53, 2015.

[118] X. Huang, Y. Wang, J. Zhang, F. Wu, and Y. Yang, "Low-temperature thermochronological insights into the Mesozoic–Cenozoic exhumation history of the Taihang–Lvliangshan region: a review," *Geological Journal*, vol. 57, no. 4, pp. 1511–1529, 2021.

[119] L. Wu, F. Wang, J. Yang, Y. Wang, and W. Shi, "Meso-Cenozoic uplift of the Taihang mountains, north China: evidence from zircon and apatite thermochronology," *Geological Magazine*, vol. 157, no. 7, pp. 1097–1111, 2019.

[120] J. Zhao, C. Liu, N. Mountney, et al., "Timing of uplift and evolution of the Lüliang mountains, north China Craton," *Science China Earth Sciences*, vol. 59, no. 1, pp. 58–69, 2016.

[121] Z. Ding, L. Wang, P. Zhang, K. Zhong, and S. Liu, "Crustal extention and fault activity during the Mesozoic-Cenozoic in the Jiyang depression and the Luxi uplift, east China," *Oil and Gas Geology*, vol. 29, no. 1, pp. 107–140, 2008.

[122] L. Li, L. Zhao, and D. Zhong, "Cenozoic continental intraplate extension basin-mountain coupling and continental collision: evidences from Bohai Bay basin, its peripheral mountain and Tancheng-Lujiang fault," *Chinese Journal of Geology*, vol. 48, no. 2, pp. 406–418, 2013.

[123] Y. Zhu, S. Liu, B. Zhang, M. Gurnis, and P. Ma, "Reconstruction of the cenozoic deformation of the Bohai Bay basin, north China," *Basin Research*, vol. 33, no. 1, pp. 364–381, 2021.

[124] Z. Li, C. Xu, Y. Shi, and Y. Li, "Discovery of detrital high-pressure metamorphic minerals from Paleocene-Eocene strata in Jiyang basin, eastern north China, and its implication for Tectonic-Paleogeographic setting," *Acta Petrologica Sinica*, vol. 25, no. 12, pp. 3130–3140, 2009.

[125] Y. Shi, Z. Li, X. Bu, and C. Xu, "Detrital garnets from Cenozoic sandstones across boxing sag for provenace indicator and its implication for the Luxi uplift," *Acta Sedimentologica Sinica*, vol. 27, no. 5, pp. 967–975, 2009.

[126] G. Zong, H. Xiao, C. Li, Y. Shi, and L. Wang, "Evolution of Jiyang depression and its tectonic implications," *Geological Journal of China Universities*, vol. 5, no. 3, pp. 275–282, 1999.

[127] J. Qi and Q. Yang, "Cenozoic structural deformation and dynamic processes of the Bohai Bay basin province, China," *Marine and Petroleum Geology*, vol. 27, no. 4, pp. 757–771, 2010.

[128] J. Liang, H. L. Wang, Y. Bai, X. Y. Ji, and X. M. Duo, "Cenozoic tectonic evolution of the Bohai Bay basin and its coupling relationship with pacific plate subduction," *Journal of Asian Earth Sciences*, vol. 127, pp. 257–266, 2016.

[129] S. Liu, M. Gurnis, P. Ma, and B. Zhang, "Reconstruction of northeast Asian deformation integrated with western pacific plate subduction since 200 Ma," *Earth-Science Reviews*, vol. 175, pp. 114–142, 2017.

[130] S. Li, G. Zhao, L. Dai, et al., "Cenozoic faulting of the Bohai Bay basin and its bearing on the destruction of the eastern north China Craton," *Journal of Asian Earth Sciences*, vol. 47, pp. 80–93, 2012.

[131] F. Yang, M. Santosh, and S. W. Kim, "Mesozoic magmatism in the eastern north China Craton: insights on tectonic cycles associated with progressive Craton destruction," *Gondwana Research*, vol. 60, pp. 153–178, 2018.

[132] G. Zhu, D. Jiang, B. Zhang, and Y. Chen, "Destruction of the eastern north China Craton in a backarc setting: evidence from crustal deformation kinematics," *Gondwana Research*, vol. 22, no. 1, pp. 86–103, 2012.

[133] R. K. Ludwig, "Isoplot; a plotting and regression program for Radiogenic-Isotope data; version 2.53," Open-File Report 91, 1991.

[134] R. D. Müller, M. Seton, S. Zahirovic, et al, "Ocean basin evolution and global-scale plate reorganization events since Pangea breakup," *Annual Review of Earth and Planetary Sciences*, vol. 44, no. 1, pp. 107–138, 2016.